# POLITECNICO DI TORINO
## Repository ISTITUZIONALE

CFD simulation of a high-shear mixer for food emulsion production

(Article begins on next page)

20 March 2024

# CFD simulation of a high-shear mixer for food emulsion production

Marco Ferrari[a], Gianluca Boccardo[a,*], Antonio Buffo[a], Marco Vanni[a] and Daniele L. Marchisio[a]

[a]*Department of Applied Science and Technology, Politecnico di Torino, Corso Duca degli Abruzzi 24, Torino, 10129, Italy*

## ARTICLE INFO

## ABSTRACT

Mayonnaise is a stable liquid-liquid emulsion with high content of the dispersed oil phase. In the last step of its production, the emulsion is fluxed into a high-shear mixer, where the oil droplets undergo breakage until the final size distribution is reached. This step is crucial to fine-tune the droplet size distribution (DSD), in order to result in the desired structure, stability, taste, and color. In this work, we aim to model this last step via computational fluid dynamics (CFD) and population balance modeling (PBM), to properly describe both the non-Newtonian dynamics of the emulsion and the evolution of the DSD. 2D and 3D CFD simulations show that attention should be paid to the grid resolution to properly describe recognizable patterns observed in experiments. Moreover, CFD and PBM simulations clarify the role of the pre- and post-mixing zones in the high-shear mixer, as well as the effect of the type of flow, pure shear vs elongational, on droplet breakage. We thus propose a physics-based model as a computational tool in order to possibly develop a digital twin of the industrial food emulsion preparation.

## 1. Introduction

Emulsions are constituted of two immiscible liquid phases of which one is dispersed in the form of drops. Mayonnaise, the food emulsion investigated in this work, is made of a continuous aqueous phase and a dispersed phase with high content of oil. The stability of the dispersion is provided by molecules present in the egg yolk that act as surfactants and accumulate at the oil-water interface preventing the coalescence of the oil droplets. The droplet size distribution (DSD) is the most important property of the emulsion since it determines the structure, stability, taste, and color of the final product (McClements, 2005). The DSD in turn depends on the composition of the system, the type of process, and the operating conditions in which the production process operates (Walstra, 1993). In general, the production of emulsions is based on mixing the ingredients and applying enough mechanical energy to reach the desired DSD. In the case of mayonnaise, this is accomplished by first mixing the ingredients (mainly egg yolk, vinegar, oil, and water) in large stirred vessels at moderate rotational speed, and subsequently feeding such premixed emulsion into a high-shear device. Several high-shear devices are used in the process industry (Icardi et al., 2011; Lince et al., 2011; Marchisio et al., 2008; Vashisth et al., 2021) and for emulsions a popular option is the cone mill mixer, where the oil droplets undergo breakage until the final DSD is reached. This last step is crucial to fine-tune the DSD, in order to determine the properties of the final product.

---

*Corresponding author

✉ gianluca.boccardo@polito.it (G. Boccardo)
ORCID(s):

A typical cone mill mixer is constituted of a solid conical frustum rotor inside a slightly larger stator of the same shape, forming a small gap in which the emulsion flows and experiences high shear stresses, due to the high rotational speed of the rotor. The emulsion, before transiting through the high-shear region, flows into a pre-mixing chamber, followed by a post-mixing chamber.

Over time several attempts to model the DSD of mayonnaise have been made (Almeida-Rivera and Bongers, 2010; Dubbelboer, 2016; Dubbelboer et al., 2016; Maindarkar et al., 2014; Wieringa et al., 1996), but there are still many issues that need to be completely understood. For example, in the range of shear stresses developed inside the cone mill, highly concentrated emulsions show non-Newtonian dynamics, depending on both the oil content and the DSD, that need to be accounted for (Barnes, 1994; Dubbelboer, 2016). In addition, when processing very viscous liquids the cone mill operates in the laminar regime; however, a simple Poiseuille-Couette flow field can undergo a transition to the Taylor-Couette regime above a critical operating condition (Li et al., 2010, 2014; Noui-Mehidi et al., 2005; Wimmer, 2000; Wimmer and Zierep, 2000), where counter-rotating toroidal vortices (also known as Taylor vortices) appear. Since the transition to Taylor vortices depends strongly on the geometry of the system (Wimmer, 2000) and the contribution of the axial flow component that has a stabilizing effect on the formation of these instabilities (Giordano et al., 1998), a detailed flow field analysis must be carried out in order to predict the occurrence of these peculiar flow patterns. Previous modeling efforts focused on the high-shear zone in the cone mill, while the role of the pre- and post-mixing zones, before and after the high-shear region, was not investigated (Dubbelboer et al., 2016; Janssen and Hoogland, 2014; Maindarkar et al., 2014; Vashisth et al., 2021), neglecting their effect on the final drop size. Moreover, the influence of the local type of flow on drop breakage, namely pure-shear versus elongational, is not completely clear (Lupieri et al., 2021; Zinchenko and Davis, 2015).

Here, we aim to model this last step of the mayonnaise production process in a cone mill by means of 2D and 3D computational fluid dynamics (CFD) simulations and population balance modeling (PBM) in order to: (1) properly describe the non-Newtonian dynamics of the emulsion, (2) investigate the role of the pre- and post-mixing zones and (3) clarify the importance of the local type of flow. In particular, although mayonnaise consists of two distinct phases, high internal phase emulsions can be considered as a shear-thinning pseudo-single phase system with an apparent density and viscosity. Although neglecting the distinct characteristics of both oil and water may lead to inaccurate predictions (Li et al., 2015), many previous works modeled highly concentrated emulsions showing a shear thinning non-Newtonian rheological behavior as a pseudo-single phase (Alade et al., 2020; Bulgarelli et al., 2021; Dubbelboer et al., 2016; Goodarzi and Zendehboudi, 2019; Janssen and Hoogland, 2014). This hypothesis is consistent and strictly related to the mean field model, which assumes simply that the breakup of a droplet in a concentrated emulsion is determined by the average emulsion viscosity rather than the continuous phase viscosity (Jansen et al., 2001). The apparent emulsion viscosity, as a function of oil content, was evaluated through fitting of experimental data, by using a

power law model with a plateau at the high shear rate end (Dubbelboer, 2016). In order to describe the evolution of the DSD, the Population Balance Equation (PBE) is employed, in which the coalescence and breakage of the oil droplets are taken into account by appropriate kernels, which in turn depend on the local flow conditions, which range from rotation to pure-shear and finally to elongation, depending on the relative contribution of rotation and strain. In fact, while the gap section mostly exhibits a simple shear flow, a component of elongational flow is expected in the pre- and post-chambers of the cone mill that may contribute to the droplet breakage (Maffettone and Minale, 1998). Previous PBM were not capable of providing accurate predictions due to their restrictive assumptions, since coalescence was neglected (Almeida-Rivera and Bongers, 2010; Wieringa et al., 1996). In fact, although cone mills are designed to promote drop breakage, colliding droplets may coalesce under certain conditions (Maindarkar et al., 2014, 2012). Moreover, the individual and combined influence of the local type of flow (simple shear and elongational) on the final drop size can be elucidated by suitably applying a more accurate method for the solution of the PBM. Here, the Quadrature Method of Moments (QMOM) (Lavino et al., 2021; Marchisio and Fox, 2013; Marchisio et al., 2003a,b; Mazzei et al., 2012; McGraw, 1997; Sierra-Pallares et al., 2012) is used in order to solve the PBE, whereas CFD simulations are performed with the open source CFD code OpenFOAM (version 6.0) (Buffo et al., 2016b; Passalacqua et al., 2018).

This paper is organized as follows: Section 2 summarizes the main equations used to describe the flow field and the DSD evolution, Section 3 reports the details about the simulation test cases and their implementation into OpenFOAM, Section 4 focuses on the most important results obtained, and finally Section 5 presents the main conclusions of this work.

## 2. Theoretical background

The emulsification within the rotor-stator system investigated in this work is a steady-state process. Therefore, the well-known momentum balance equation for an incompressible, non-Newtonian, and stationary flow is solved in order to obtain the flow field (Bird et al., 1960). In this geometry, the centrifugal force that acts on the rotating fluid is not perpendicular to the surfaces of the rotor and stator. The flow field between two coaxial conical cylinders can present instabilities, known as Taylor vortices (Wimmer, 2000). These vortices are superimposed to the main Couette flow with an axial throughput (Giordano et al., 1998). For such a particular system, very different flow patterns can develop inside the cone mill with varying operating conditions (Noui-Mehidi et al., 2005); however, as it will be shown in Section 4, the conditions investigated in this work only result in the appearance of laminar Taylor vortices. Therefore, the implementation of a turbulence model is not necessary since the cone mill is designed to operate under laminar conditions when processing very viscous liquids that exhibit a shear thinning non-Newtonian rheological behavior like

78  mayonnaise (McClements, 2005). This condition is also verified here in line with previous works (Dubbelboer et al.,

79  2016; Lupieri et al., 2021).

80  In order to evaluate this particular flow pattern, the Reynolds number in the cone mill gap is calculated as follows:

$$\mathrm{Re_{gap}} = \frac{\omega R_{max} d}{\langle \nu_{emul} \rangle}, \tag{1}$$

81  where $\omega$ is the angular velocity of the rotor and $d$ is the distance (gap) between the rotor and the stator. In general, the

82  Reynolds number for the investigated system is not constant, since the rotor radius increases from the top to the bottom

83  of the cone mill and the viscosity changes locally as a function of the local shear rate $\dot{\gamma}$. Therefore, the maximum rotor

84  radius $R_{max}$ and the volume-averaged kinematic apparent viscosity of the emulsion $\langle \nu_{emul} \rangle$ are used in Equation (1).

85  This corresponds to the definition used in previous simulation works with whose results we compared our work. For

86  specific operating conditions, it is a good approximation to only consider the volume average of the emulsion viscosity

87  $\langle \nu_{emul} \rangle$, since the local shear rate inside the gap section of the cone mill mostly depends on the tangential velocity

88  gradient. As it will be shown in Section 4, the tangential component of velocity shows a linear profile (and a constant

89  gradient) along the gap width for a specific rotor radius. On the other hand, along the height of the cone mill, there are

90  just small variations of the tangential velocity gradient, since the difference between the maximum and the minimum

91  rotor radius is small (see Figure 2).

92  As regards the pre- and post-mixing zones, the Reynolds number is defined instead as $\mathrm{Re} = \langle U \rangle d_{max}/\langle \nu_{emul} \rangle$,

93  where $U$ is the velocity magnitude, $d_{max}$ is the maximum cone mill diameter of the pre- and post-mixing zones, while

94  the symbol $\langle \cdot \rangle$ indicates a volume-average in the pre- and post-chamber of the cone mill (for $\mathrm{Re_{pre}}$ and $\mathrm{Re_{post}}$ in Table

95  1, respectively).

## 2.1. Non-Newtonian rheology model

97  In order to properly describe the non-Newtonian dynamics of the emulsion, the fluid is considered as a shear-

98  thinning pseudo-single phase system, with an apparent emulsion viscosity $\eta_{emul}$ evaluated through a power law model

99  with a plateau at high shear rates fitted with experiments and reasonably accurate in the range of the local shear rate $\dot{\gamma}$

100  developed inside the cone mill mixer ($10^3 - 10^5 s^{-1}$) (Dubbelboer, 2016; Dubbelboer et al., 2016):

$$\frac{\eta_{emul}}{\eta_c} = \eta_r = \eta_{r,\infty} + K\dot{\gamma}^m. \tag{2}$$

101  In Eq. (2), $\eta_r$ is the dimensionless relative viscosity, expressed as the ratio of apparent emulsion viscosity $\eta_{emul}$ to

102  continuous water phase viscosity $\eta_c$. The continuous phase consists of egg yolk, salt, and vinegar dissolved in water,

103  and its viscosity was measured to be Newtonian over the range of shear rates investigated and equal to $10 \, \mathrm{mPa \cdot s}$

(Dubbelboer, 2016; Dubbelboer et al., 2016). In Eq. (2), $\eta_{r,\infty}$ is the relative plateau viscosity for high shear rates. The parameters $\eta_{r,\infty}$, $K$, and $m$ result from experimental data fitting and they only depend on the oil concentration (Dubbelboer, 2016). The kinematic apparent emulsion viscosity is $\nu_{emul} = \eta_{emul}/\rho_{emul}$, where $\rho_{emul}$ is the apparent emulsion density, calculated as $\rho_{emul} = \rho_{oil}\phi_v/\phi_w$. Here, $\phi_v$ and $\phi_w$ are respectively the oil volume and the oil weight fractions, as reported in the reference experimental work (Dubbelboer, 2016; Dubbelboer et al., 2016). It is important to point out here that Dubbelboer (2016); Dubbelboer et al. (2016) provided a relationship for the apparent emulsion viscosity as a function of the equilibrium mean oil droplet diameter, which instead is a local variable in this work. Therefore, the relation expressed in Eq. (2) to describe the non-Newtonian dynamics of the emulsion is employed here in order to make viscosity locally varies with the shear rate within the cone mill and to be intrinsically dependent on the DSD through the experimental fitting parameters themselves. It is also important to point out that emulsions can generally be treated as pseudo-homogeneous fluids with averaged properties as the dispersed droplets of emulsions are small and well distributed (Chhabra and Richardson, 2008; Pal, 1993; Pal and Hwang, 1999), leading to two key assumptions to be fulfilled: the continuum description and the homogeneity. The former is valid when the distribution of particles in the liquid phase is not influenced by the channel dimensions. In this work, the largest oil droplets are around 10 times smaller than the gap section, so it is reasonable to consider the DSD independent of cone mill geometry. Secondly, the homogeneity leads to the use of space-averaged fluid properties. This can be valid when the emulsion is stabilized by surfactants, so no phase transition occurs. Here, the emulsion was pre-mixed together with the main ingredients including egg yolk surfactants in a previous production step. Thus, oil droplets were already stabilized and a coarse inlet DSD is fluxed into the cone mill.

## 2.2. CFD and PBM description

As mentioned, the flow field of the liquid-liquid emulsion in the cone mill is described by solving the steady-state continuity and momentum balance equations for an incompressible pseudo-single phase non-Newtonian flow, as detailed in previous works (Boccardo et al., 2014; Tosco et al., 2013). By solving these equations the emulsion velocity in the cone mill, $\mathbf{U}$, described as a pseudo-single phase fluid, is calculated. Numerous interesting flow features can be extracted via this variable. For example, the local shear rate is calculated as follows:

$$\dot{\gamma} = 2\sqrt{II_{\mathbf{E}}}, \tag{3}$$

where $II_{\mathbf{E}}$ is the second invariant of the symmetric rate-of-strain tensor $\mathbf{E}$, which is in turn defined as:

$$\mathbf{E} = \frac{1}{2}\left[\nabla\mathbf{U} + (\nabla\mathbf{U})^T\right]. \tag{4}$$

₁₃₀ Another interesting flow feature is the so-called Manas-Zloczower mixing index, defined as follows:

$$\alpha = \frac{\sqrt{II_{\mathbf{E}}}}{\sqrt{II_{\mathbf{E}}} + \sqrt{II_{\mathbf{\Omega}}}}, \tag{5}$$

₁₃₁ where $II_{\mathbf{\Omega}}$ is the second invariant of the skew-symmetric rate-of-rotation tensor $\mathbf{\Omega}$, which in turn is defined as:

$$\mathbf{\Omega} = \frac{1}{2} \left[ \nabla \mathbf{U} - (\nabla \mathbf{U})^T \right]. \tag{6}$$

₁₃₂ The mixing index $\alpha$ has a 0-1 range, with 0 indicating a rotational motion, and 0.5 and 1 indicating pure shear and
₁₃₃ pure elongational flows, respectively (Frungieri et al., 2022, 2020). As we will see both $\dot{\gamma}$ and $\alpha$ play an important role
₁₃₄ during droplet breakup.

₁₃₅ The evolution of the droplet size distribution (DSD) is properly described by the PBE, accounting for the birth and
₁₃₆ death of droplets due to coalescence and breakage. Assuming the emulsification process at steady-state and omitting
₁₃₇ explicit indications of space and time dependencies, the PBE can be written as follows (Ramkrishna, 2000):

$$\nabla \cdot (\mathbf{U}\, n(L)) = \frac{L^2}{2} \int_0^L \frac{C\left(\left(L^3 - L'^3\right)^{1/3}, L'\right)}{\left(L^3 - L'^3\right)^{2/3}} n\left(\left(L^3 - L'^3\right)^{1/3}\right) n\left(L'\right) dL'$$
$$- n(L) \int_0^\infty C\left(L, L'\right) n\left(L'\right) dL' + \int_L^\infty g\left(L'\right) \beta\left(L|L'\right) n\left(L'\right) dL' - g(L)n(L), \tag{7}$$

₁₃₈ where $n(L)$ is the DSD (Marchisio and Fox, 2013), $L$ is the droplet diameter as well as the internal coordinate of the
₁₃₉ PBE. The coalescence kernel, $C(L, L')$, and the breakage kernel, $g(L)$, quantify the rate with which droplets coalesce
₁₄₀ and break. The daughter distribution function, $\beta(L|L')$, defines instead the size distribution of the droplets formed by
₁₄₁ the breakup of a droplet of size $L'$.

₁₄₂ Thanks to the assumption of considering the emulsion as a shear-thinning pseudo-single phase, $\mathbf{U}$ in Eq. (7) is
₁₄₃ the fluid velocity obtained by solving the flow field equation (as explained above). Therefore, $\mathbf{U}$ represents the first
₁₄₄ coupling variable used in this work, and from the flow field, it is possible to calculate the local shear rates $\dot{\gamma}$ (Bird
₁₄₅ et al., 1960). The right-hand side of Eq. (7) is the source term due to the coalescence and breakage of the oil droplets,
₁₄₆ which are described by means of phenomenological models called kernels (Li et al., 2017). As previously mentioned,
₁₄₇ in this work QMOM (Marchisio et al., 2003a,b) is employed to solve the PBM (Equation (7)). The general idea behind
₁₄₈ this method is to solve transport equations for the moments of the DSD. By approximating the unknown DSD, $n(L)$,
₁₄₉ as a summation of Dirac functions and using a quadrature approximation of order $N$, QMOM leads to the following

expression for the moment of order $k$ (Marchisio et al., 2003b):

$$M_k = \int_0^{+\infty} n(L)L^k \mathrm{d}L \approx \sum_{\alpha=1}^{N} w_\alpha L_\alpha^k \quad \text{with} \quad k \in 0, ..., 2N-1, \tag{8}$$

where $w_\alpha$ and $L_\alpha$ are the $N$ quadrature weights and $N$ quadrature abscissas, in turn calculated from the first $2N$ lower-order moments through so-called moment inversion algorithms, such as the Product-Difference (PD) (Marchisio and Fox, 2013) algorithm employed in this work. The reader can refer to the literature for further details (Boccardo et al., 2019; Li et al., 2017; Marchisio and Fox, 2013; Marchisio et al., 2003a,b; McGraw, 1997). Moreover, it is important to remark that the moments represent integral properties of the DSD. For example, in the case investigated here, $M_0$ represents the number of oil droplets per unit volume, while $M_3$, if multiplied by a shape volume coefficient equal to $\pi/6$ due to spherical shape of the droplets, is equal to the oil volume fraction. Most importantly, the mean Sauter diameter used in this work for evaluating the evolution of the DSD is simply defined as follows: $d_{32} = M_3/M_2$.

The coupling between CFD and PBM is realized here by using two approaches. Some of the simulations are run with the classical on-the-fly coupling, where the governing equations are solved simultaneously (Gao et al., 2016), whereas another part of the simulations is run with the off-line coupling, where first the CFD equations for the flow field are solved, the relevant information for the flow field is extracted (i.e. shear rate and mixing index) and finally a volume-averaged PBM is solved for the evolution of the DSD (Buffo et al., 2016a; De Bona et al., 2016).

Three important functions appear which determine the evolution and the final shape of the DSD: the coalescence kernel $C(L, L')$, the breakage kernel $g(L)$, and the daughter-size distribution function $\beta(L|L')$. The coalescence kernel $C(L, L')$, quantifying the rate of coalescence of droplets of diameter $L$ and $L'$, and the breakage kernel $g(L)$, quantifying the rate of breakage of droplets of size $L$, take respectively the following forms (Maindarkar et al., 2014):

$$C(L, L') = K_1 \frac{\pi}{6} \left( \frac{\dot{\gamma}}{1 - \phi_v} \right) (L + L')^3 \exp\left( -K_2 \lambda \mathrm{Ca}^{\frac{3}{2}} \left( \frac{8\pi\sigma R_{eq}^2}{A_H} \right)^{\frac{1}{3}} \right),$$
$$g(L) = K_3 \dot{\gamma} \exp\left( -K_4 \frac{\mathrm{Ca_{cr}}}{\mathrm{Ca}} \right), \tag{9}$$

where $\phi_v$ is the oil volume fraction, $A_H$ is the Hamaker constant, $\lambda$ is the ratio between the oil viscosity $\eta_{oil}$ and the apparent emulsion viscosity $\eta_{emul}$, and $K_1$, $K_2$, $K_3$, and $K_4$ are free adjustable model parameters to be fitted with experimental data. $R_{eq}$ is the equivalent radius of colliding drops of diameter $L$ and $L'$, defined as: $R_{eq} = 2/(2/L + 2/L')$. Although the interfacial tension $\sigma$ in Eq. (9) is dynamic for an oil-in-water emulsion as it varies according to local flow conditions (Anton, 2013), it is here assumed constant and equal to 10 mN/m as in the work of Dubbelboer et al. (2016) and verified in previous studies (Ferrari et al., 2023, 2022). In Eq. (9), Ca is the

capillary number, defined as:

$$\mathrm{Ca} = \frac{\eta_{emul}\dot{\gamma}L}{2\sigma},$$

(10)

where $\eta_{emul}$ is the apparent emulsion viscosity and $\dot{\gamma}$ is the local shear rate.

The high shear rates developed inside the mixer tend to stretch the oil droplets and droplet breakage is assumed to follow the capillary instability mechanism. This means that, when the ratio of the viscous stress acting on the drops to the interfacial tension force, i.e. Ca, exceeds a critical value, i.e. the critical capillary number $\mathrm{Ca}_{cr}$, a mother droplet breaks into two or more daughter droplets, depending on the form of the daughter-size distribution function $\beta(L|L')$. The critical capillary number $\mathrm{Ca}_{cr}$ determines the stability of the droplet and depends on the ratio between the viscosity of the disperse and continuous phases, $\lambda$, and on the type of flow inside a specific geometry (Bentley and Leal, 1986; Frungieri and Briesen, 2023). Its expression can usually be derived from experiments and in this work, we used two empirical correlations. The first one refers to the case of pure shear flow (i.e. mixing index, $\alpha$, equal to 0.5) (Debruijn, 1991) as the result of single droplet breakup experiments between two concentric cylinders:

$$\log_{10}\mathrm{Ca}_{cr} = -0.506 - 0.0994\log_{10}\lambda + 0.124(\log_{10}\lambda)^2 - \frac{0.115}{\log_{10}\lambda - 0.611}.$$

(11)

It is worth mentioning that this expression is valid for $\lambda < 4$, as for $\lambda > 4$ the critical capillary number tends to infinity, implying that for $\lambda > 4$ pure shear flow is not effective in breaking the droplets. The second one refers to the case of flows with an elongational component (i.e. $0.5 < \alpha \leq 1.0$) and reads as follows (Bentley and Leal, 1986):

$$\mathrm{Ca}_{cr} = \frac{0.14\lambda^{-1/6}}{\alpha^{1/2}},$$

(12)

Figure 1 reports the dependency of the critical Capillary number versus the viscosity ratio for two values of the mixing index, namely pure shear flow, $\alpha = 0.5$, and pure elongational flow $\alpha = 1.0$. As it is seen, for every reported value of the viscosity ratio $\lambda$, the critical Capillary number for pure elongational flow is smaller than for pure shear flow, indicating that flows with an elongational component are more effective in breaking droplets. This is particularly true for highly viscous disperse phases, where $\lambda > 4$. In these cases in fact the critical Capillary number for pure shear flows is practically infinitely large, implying that pure shear flow cannot break the droplets, no matter how intense is the shear rate. When $\lambda > 4$ only an elongational component can reduce the drop size.

As far as the viscosity ratio, $\lambda = \eta_d/\eta_c$, is concerned, this is usually evaluated as the ratio between the dispersed and continuous phase viscosity. It is however very common, in the case of dense emulsions, to use the apparent emulsion viscosity $\eta_{emul}$ instead of the continuous phase viscosity $\eta_c$, as in high disperse phase emulsions, droplets perceive a

198 surrounding continuous phase with the emulsion viscosity (Jansen et al., 2001; Maindarkar et al., 2014). This is also

199 consistent with simulating the flow field in the device by using the pseudo-single phase approach.

200    The coalescence kernel $C(L, L')$ in Eq. (9) is incorporated in the model since colliding drops may coalesce despite

201 the cone mill is designed to promote droplet breakage (Maindarkar et al., 2014, 2012). The coalescence kernel which

202 depends on colliding drops of diameter $L$ and $L'$ appears in the PBE (Eq. (7)), thus affecting the evolution and the

203 final shape of the DSD. The coalescence rate is determined by the product of the frequency of droplet collisions and

204 the probability that a collision event will produce coalescence. The collision frequency depends on the local flow

205 field (Klink et al., 2011), and the coalescence probability depends on the capillary number Ca and the viscosity ratio

206 $\lambda$ (Chesters, 1991). Further details about the expressions of kernels used in this work can be found in the literature

207 (Dubbelboer, 2016; Dubbelboer et al., 2016; Maindarkar et al., 2014). As it can be seen from Eqs. (9) to (12), the

208 coalescence and the breakage kernels are calculated as functions of the local shear rate $\dot{\gamma}$ and of the local apparent

209 emulsion viscosity $\eta_{emul}$, both resulting from solving the flow field.

210    Regarding the daughter-size distribution $\beta(L|L')$, it states the size distribution of daughter droplets originating

211 from a mother droplet after a breakage event. Here a beta function is employed (Laakkonen et al., 2006):

$$\beta(L, L') = 180\left(\frac{L^2}{L'^3}\right)\left(\frac{L^3}{L'^3}\right)^2\left(1 - \frac{L^3}{L'^3}\right)^2, \tag{13}$$

212 where $L$ and $L'$ are the sizes of the daughter and mother droplets. Equation (13) assumes that two droplets are formed

213 from a mother and that symmetric breakage is the most likely event. It is important to remind here that the choice of the

214 daughter-size distribution function has a large impact on the final DSD (Dubbelboer, 2016; Dubbelboer et al., 2016;

215 Maindarkar et al., 2014), but much less on the mean Sauter diameter (Gao et al., 2016), used to evaluate the evolution

216 of the DSD in this work. Therefore, the form of the daughter-size distribution function is of secondary importance

217 here.

## 3. Numerical details

219    As already mentioned, we simulated the last step of the mayonnaise production process, i.e., the cone mill mixer,

220 by using CFD and PBM as described in Section 2. The information about the experiments is taken from the work of

221 Dubbelboer (2016); Dubbelboer et al. (2016). More in detail, three types of mayonnaise were prepared with different

222 concentrations of soybean oil (0.65, 0.70, 0.75 kg/kg), whose density $\rho_d$ and viscosity $\eta_d$ are respectively equal to 917

223 kg/m$^3$ and 50 mPa · s (Maindarkar et al., 2014). Before pumping it into the cone mill, the mayonnaise is characterized

224 by a coarse DSD, whose shape only depends on the initial oil content. After the continuous mixing process into the

cone mill, the desired product structure is obtained, i.e. the final DSD is reached. Upstream and downstream DSD measurements are available in the literature for model validation.

Each one of these three types of mayonnaise was processed under the three different operating conditions reported in Table 1. The last three columns report the corresponding Reynolds numbers for the intermediate soybean oil concentration (0.70 kg/kg). As it can be seen, only for experiment 1 the Reynolds number in the gap section exceeds the critical Reynolds number (also corresponding to the highest Taylor number), highlighting for this operating condition the presence of Taylor vortices (Li et al., 2010, 2014) (see Section 4.1).

A sketch of the cone mill mixer, together with its 2D and 3D representations, is reported in Figure 2. It consists of a solid conical frustum rotor, which rotates clockwise inside a slightly larger stator of the same shape. This configuration forms a small gap in which the emulsion flows from the top to the bottom of the cone mill. The chambers before and after the small gap ensure a homogeneous composition of the emulsion but their role in determining the final DSD is not fully clear (Dubbelboer, 2016; Dubbelboer et al., 2016; Lupieri et al., 2021). This is why we considered different geometries for the simulations, including 2D and 3D representations of the gap region, with and without the pre- and post-mixing chambers. Finally, it is worth mentioning that the pilot scale apparatus (manufactured by IKA) employed in experimental measurements has a more complex geometry, but the representation reported in Fig. 2 is a reasonable compromise between computational costs and accuracy (Dubbelboer, 2016).

All the simulations were performed with the open-source CFD software OpenFOAM (version 6.0). In order to evaluate the flow field, the SRFSimpleFoam solver is employed, which is a steady-state solver for incompressible flows in a single rotating frame. This solver adopts the SIMPLE algorithm for the solution of velocity and pressure coupling. The viscosity model of the emulsion described in Section 2.1 is implemented as an add-on library.

In order to properly describe the flow field in the cone mill a grid independence study has been conducted. The six different grids described in Table 2 were tested. These six grids refer to the 2D geometry limited to the gap, without pre- and post-mixing chambers. The Table reports the grid resolution along the axial and radial directions, the total number of cells, the resulting number of Taylor vortices, and the volume-averaged shear rate. Only the fine resolution of Grids 4, 5, and 6 makes it possible to properly describe the flow field, both in terms of the number of Taylor vortices and volume-averaged shear rate. Similar information is reported in Fig. 3 where a contour plot of the shear rate is reported for Experiment 1 and an oil concentration of 0.65 kg/kg for Grid 1 and Grid 4. As it is seen the vortex structures emerge and are correctly described only at the second grid resolution. Moreover, for the six grid resolutions of Table 2, Fig. 4 reports the volume probability density distributions (PDF) of the values of pressure $p$ normalized with respect to the atmospheric pressure $p_{atm}$, relative viscosity $\eta_r$, and shear rate $\dot{\gamma}$ normalized with respect to the nominal shear rate $\dot{\gamma}_n$ calculated as the rotor maximal tip velocity divided by the gap size. As it can be seen, the finer the grid resolution the better defined the shape of the distributions. Therefore, all subsequent results refer to a grid resolution of at least

25 × 360 cells in the gap, corresponding to Grid 4 (red highlighted curves in Fig. 4), as a compromise between result accuracy and computational cost.

The PBM is solved by means of the QMOM with a three node quadrature, meaning that the first six moments of the DSD are transported. Although in general the evolution of the DSD has an effect on the emulsion viscosity (Barnes, 1994), the rheology model here implemented depends only on the disperse phase volume fraction and not on the oil droplets size. Therefore the hydrodynamics of the emulsion does not depend on the DSD (see Section 2.1). As a consequence, in all simulations at first, only the governing equations of SRFSimpleFoam are solved, in order to obtain a steady-state flow field information. Then, the variables linking CFD and PBM together, i.e. viscosity and velocity fields (see Section 2.2), are transferred to the PBM model. As mentioned, in this work two approaches are used; for a limited number of cases, the viscosity and velocity field are transferred to the modified scalarTransportFoam in order to solve the PBM, within the CFD code but assuming the flow field was frozen. Further details about this implementation can be found in our previous works (Boccardo et al., 2019; Buffo et al., 2013, 2016b; Passalacqua et al., 2018). Here, the six moments are considered as scalars and their transport equations are incorporated in the scalarTransportFoam module of OpenFOAM that provides a solver for steady or transient transport equation for a single passive scalar, obtaining a modified solver for the solution of the six equations simultaneously. The coalescence and breakage kernels described in Section 2.2 are used to evaluate the droplet coalescence and breakage rates. Alternatively, the shear rate, $\dot{\gamma}$, and the mixing index, $\alpha$, within the cone mill are extracted and the PBM is solved in a simplified form as described in previous works (De Bona et al., 2016).

An overview of the numerical schemes and of the boundary conditions used in this work can be found in Table 3. Regarding inlet boundary conditions, the zero gradient condition is set for the pressure, whereas for the velocity an inlet constant profile is imposed, whose value is calculated from the inlet mass flow rate corresponding to experiments reported in Table 1. The values of inlet moments (and consequentially the inlet $d_{32}$ value) are calculated from the experimentally measured inlet DSD.

## 4. Results and discussion

In this section, the most significant results of the simulations performed will be presented. First, the flow field of the emulsion inside the mixer is shown, then, the results of the PBM simulations are also discussed and compared with experimental data.

### 4.1. Flow field results

It is interesting to compare the CFD results obtained with the 2D and 3D geometries with the pre- and post-mixing chambers. Figure 5 reports this comparison in terms of the axial velocity across the gap for three different axial positions

(inlet, center, and outlet) for one operating condition, namely experiment no. 1 of Tab. 1. As it is seen, no significant difference is observed between the 2D and the 3D predictions, probably due to the intrinsic axial symmetry of the cone mill. For this reason from now on only 2D results will be presented and discussed. Figs. 6 and 7 qualitatively represent the flow field developed within the cone mill. The streaklines for one operating condition are reported in Fig. 6. As it is seen two large laminar recirculation zones are identified in the pre- and post-mixing chambers. Such a secondary flow pattern is due to the sudden presence of a very narrow gap between the top and bottom chambers. This is correctly reproduced as in the work of Lupieri et al. (2021), where its effect was extensively discussed. Moreover, similar results were obtained in terms of pressure change within the cone mill compared to those of the work of Lupieri et al. (2021), where the same emulsion was modeled with a two-phase approach, thus showing the validity of the pseudo-single phase assumption employed here.

As expected, the CFD simulations show a high velocity gradient due to the high rotational speed, in particular, the highest velocity corresponds to the tip velocity of the rotor, as it can be seen in Fig. 7, which shows the contour plot of the velocity magnitude in a magnified longitudinal section of the cone mill with oil concentration equal to 0.70 kg/kg (70 wt%) and at operating conditions corresponding to experiment no. 1.

Since the rotational speed of the rotor is considerably higher than the inlet fluid velocity, the tangential component of velocity is larger than the axial and radial one and the contour plot of the tangential velocity is very similar to the one reported in Fig. 7. Moreover, the contour plot shows that the tangential velocity has a linear profile along the gap, with the maximum value at the rotor wall and the minimum one at the stator wall, like in a Couette flow.

Although the main velocity component is the tangential one, it is more interesting to observe the trend of the axial component of the emulsion velocity ($z$-component). Figure 8 reports the axial velocity profiles versus the normalized distance from the rotor wall at half height of the cone mill, with oil concentration equal to 0.70 kg/kg (70 wt%), and for different operating conditions (see Table 1). In experiments no. 2 and 3 the axial velocity presents a parabolic profile, in which the maximum value depends on the inlet flow rate. It is worth reminding here that the fluid flow enters where the cone mill has the smaller radius (top) and exits where it has the larger one (bottom) (see Figure 2), explaining the reason for the negative values of velocity. Experiment no. 1 presents a different shape of the axial velocity. Close to the rotor wall, the axial velocity points downward, while its direction is opposite close to the stator wall. Therefore, the presence of such backflow suggests that a large vortex appears for this operating condition, extending over the entire height of the cone mill. This situation has already been observed in previous works, performed with null axial flow (Li et al., 2010, 2014). For a better understanding of the fluid flow, Reynolds numbers in the gap section (defined in Equation (1)) are calculated for the same conditions of the Figure 8, and the results are summarized in Table 1. For experiment no. 1, Re is higher than $Re_c$ (equal to 132 (Noui-Mehidi et al., 2005)), at which value the flow starts to become unstable and the first large Taylor vortex appears. Although it has been shown experimentally that the axial flow has a stabilizing

effect on the formation of instabilities, increasing the value of $Re_c$ (Giordano et al., 1998), Reynolds numbers (and, correspondingly, Taylor numbers) shown in Table 1, for experiment no. 1, is high enough to justify the axial velocity trends shown in Figure 8 and to imply the presence of a large vortex filling the entire height of the cone mill gap. Table 1 also reports the Reynolds numbers in the pre- and post-chambers of the cone mill. These values indicate that the Reynolds number is low enough to consider the flow regime laminar within the whole cone mill, despite the change in the characteristic length dimension due to the cone mill geometry. This can be justified by looking at Figure 9, showing the contour plots of the kinematic emulsion viscosity corresponding to the cases of Table 1. As it can be seen, the local viscosity in pre- and post-mixing zones is one or two orders of magnitude higher than that in the gap section. This is related to the shear-thinning behavior of the modeled emulsion (Eq. (2)) since pre- and post-mixing zones experienced much lower shear rates compared to those in the gap region.

At last, it is interesting to discuss the predictions for the shear rate, the mixing index, and the corresponding Capillary number. Figure 10 reports the contour plots for the ratio between the Capillary number and the critical Capillary number, calculated by using the emulsion viscosity and Eq. (11), and the viscosity of the continuous phase and Eq. (12), as well as the mixing index for Experiments no. 1 and 3 and an oil concentration of 0.70 kg/kg. Closer observation of Fig. 10 highlights that most of the breakage occurs in the gap, where the Capillary number is larger than its critical value, due to pure shear, namely $\alpha \approx 0.5$. Larger values of the mixing index, namely $\alpha \approx 1$, are observed in the pre- and post-mixing chambers, where however the shear rate is not large enough to ensure a value of the Capillary number greater than its critical value. This is also confirmed by the results reported in Fig. 11, where the volume distribution of shear rate and mixing index across the cone mill are reported for the three investigated operating conditions. As it can be seen, the highest shear rates ($\gamma \geq 10^3$ 1/s) are observed in regions characterized by a mixing index approximately equal to 0.5. We can therefore conclude that, although elongational flow, generally more effective in breaking droplets, is observed in the pre- and post-mixing chambers, most of the droplet breakup occurs within the cone mill gap due to pure shear.

## 4.2. PBM results

As already mentioned, the high rotational speed of the cone mill mixer develops a high-shear rate inside a narrow gap, in order to obtain the final product with the desired features.

Figure 12 reports the trend of the number of the oil droplets per unit volume, corresponding to the moment of order zero of the DSD, and the oil volume fraction, proportional to the moment of order three of the DSD, along the normalized distance from the middle point of the inlet to the middle point of the outlet of the cone mill mixer for different oil concentrations. Since the oil concentration does not change due to droplet coalescence and breakage, the third-order moment, which is proportional to the oil volume fraction, remains constant along the gap and is equal to

the corresponding values of different types of mayonnaise, as reported in a previous work (Dubbelboer et al., 2016). On the other hand, the number of oil droplets per unit volume (the moment of order zero) increases, meaning that droplets break moving through the mixer since the total oil amount is constant. In addition, it is important to note that the number of oil droplets is larger for higher oil concentrations.

The evolution of the DSD is reported in terms of the mean Sauter diameter $d_{32}$, calculated as the ratio between the third and second-order moments. Thanks to the link between PBM and CFD, as described in Section 2.2, it is possible to highlight the influence of the flow field, and in particular the high shear rates and the axial velocity, on the trend of $d_{32}$. Figure 13 reports the contour plot of $d_{32}$ along a longitudinal section of the cone mill with oil concentration equal to 0.70 kg/kg (70 wt%) for experiments no. 1 and 3. As it can be seen, $d_{32}$ decreases along the flow direction, since droplets undergo breakage induced by the high shear rates inside the mixer. These trends exactly reproduce what is expected from experimental observations (Dubbelboer, 2016; Dubbelboer et al., 2016). The insets in Figure 13 are magnified sections of the cone mill that show in detail how the flow field, and in particular the axial velocity, influences $d_{32}$ trends. For experiment n. 3, the $d_{32}$ presents a parabolic profile along the gap width, with the higher value at the center of the gap and the lower at the walls, similar to the respective axial component of velocity (see Figure 8). For experiment n. 1, the situation is different from experiment n. 3. In this case, it is represented very clearly how the flow field can influence the local DSD. As it is reported in Section 4.1 and Figure 8, the presence of Taylor instability inside the mixer leads to a particular shape of the velocity profile. Therefore, the link between CFD and PBM is able to show that the oil droplets are bigger close to the rotor and smaller close to the stator. The average outlet values of $d_{32}$ shown in Figure 13 are equal to 7.1 $\mu$m for case no. 3 and 5.4 $\mu$m for case no. 1, whereas the experimental ones are respectively 7.7 $\mu$m and 6.6 $\mu$m (Dubbelboer et al., 2016), with a relative error under 20%. These outcomes are obtained by suitably adjusting the free parameters that appear in coalescence and breakage kernels, through a trial and error procedure, and more details on this are given below. It is important to point out that the results reported here have illustrative purposes, to show the capabilities of the CFD-PBM approach. Achieving a unique and generic set of free parameters that matches all the experimental data, using optimization and uncertainty quantification techniques, will be the scope of future works.

As just mentioned the predictions of the PBM are highly affected by the values of the model parameters appearing in the coalescence kernel, $K_1$ and $K_2$, and the breakage kernel, $K_3$ and $K_4$. Due to the semi-empirical nature of these kernels and the many approximations adopted in their derivation, their values cannot be predicted by the theory but have to be fitted with experiments. An example of the influence of the model parameters on the final predictions can be found in Table 4. As expected by increasing $K_1$ coalescence becomes more important and the mean Sauter diameter increases, and conversely by increasing $K_3$ or $K_4$ breakup becomes more important and the mean Sauter diameter decreases.

In order to optimize the model parameters $K_1$, $K_2$, $K_3$, and $K_4$ the PBM, solved in the simplified form described in our previous work (De Bona et al., 2016), has been coupled with the covariance matrix adaptation evolution strategy (CMA-ES) algorithm (Hansen, 2006). The algorithm minimized the normalized distance between the predicted mean Sauter diameter and the corresponding experimental values, resulting in the final predictions reported in Table 5. The optimization was performed with the PBM implemented in its simplified form, rather than with the full CFD-PBM due to the computational costs associated with the full CFD-PBM which are prohibitive for these applications. As it can be seen from Table 5, the comparison is satisfactory as the PBM is capable of capturing the most important trends for the investigated operating conditions. The same approach was used to conduct further analysis of the individual and combined effect of the type of flow on the resulting drop size. Fig. 14 shows the comparison between the outlet experimental Sauter mean diameter values and the predicted ones for different operating conditions and mayonnaise types when droplet breakage occurs due to the simple shear, elongational flow, and the combination of both of them, respectively. As can be seen, the comparison is acceptable in the case of pure shear flow. On the other hand, the prediction is unsatisfactory when the elongational flow is only responsible for droplet breakage. However, the best results are obtained when both types of flow are taken into account (Table 5). This confirms again that simple shear flow is the most effective in droplet breakage inside the cone mill, but the combination of both shear and elongational flow gives the best predictions in terms of drop size. It is also important to point out here that the discrepancies in the results shown in the middle plot of Figure 14 are potentially due to the fact that elongational rheology is not taken into account in this work although its implementation and effect may be hard to achieve. Therefore, its study can be the object of future investigations for similar emulsions.

## 5. Conclusions

In this work, we presented a modeling approach for food emulsion production in a high-shear mixer. A flow field analysis performed with CFD shows that recognizable patterns for the investigated geometry are in agreement with previous experimental works. In particular, the tangential component of the emulsion velocity shows a Couette flow, whereas the axial velocity trends depend on Reynolds number: for $Re < Re_c$, a Poiseuille flow develops inside the gap of the mixer, but above $Re_c$ the first instability appears and backflow occurs. Thanks to the coupling between CFD and PBM, demonstrated with two approaches, it is possible to obtain a better understanding of the flow influence on the evolution of the droplet size distribution. In particular, the role of the type of flow, elongational versus pure shear, on droplet breakage and the role of the pre- and post-mixing chambers in the cone mill have been elucidated, although the emulsion elongational rheology was not taken into account here. This model accounts for both the coalescence and the breakage of the oil droplets, which depend in turn on the local flow conditions. From the evaluation of the mean oil droplet diameter, the simulations are able to show that the breaking of the oil droplets promoted by the high shear rates

prevails over the coalescence phenomenon, reproducing correctly the experimental data. As a powerful and convenient method for such kind of applications, QMOM is employed for the solution of the population balance equation, taking into account the actual hydrodynamics of the emulsion in order to provide a more accurate prediction of the droplet size distribution.

The results presented here will also serve as the basis for future extension of this work in several directions. First, an optimization procedure will be employed in order to identify an accurate and generic set of kernel constants reproducing the available experimental data. Then, these simulations can be included in a more general multi-scale framework in which the effect of the DSD on the emulsion viscosity can be taken into account via detailed interface-tracking simulations, in which the rheology of the whole emulsion is one of the possible outcomes, and the interfacial tension can be directly computed with the help of atomistic techniques, such as molecular dynamics or dissipative particle dynamics. Other aspects should also be taken into consideration when modeling the food emulsion preparation, such as a more complex geometry of the rotor-stator mixer, a better definition of the coalescence and breakage functions for highly concentrated emulsion, or the inclusion of the surfactant adsorption mechanism on the oil/water interface during droplet formation.

## Acknowledgments

### Financial disclosure

### Conflict of interest

The authors declare no potential conflict of interest.

## References

Alade, O.S., Al-Ashehri, D.A., Mahmoud, M., Sasaki, K., Sugai, Y., 2020. Evaluation of laminar flow of surfactant-stabilized bitumen-in-water emulsion in pipe using computational fluid dynamics: Effects of water content and salinity. Journal of Dispersion Science and Technology 41, 1105–1117. URL: `https://doi.org/10.1080/01932691.2019.1614046`, doi:`10.1080/01932691.2019.1614046`.

Almeida-Rivera, C., Bongers, P., 2010. Modelling and experimental validation of emulsification processes in continuous rotor–stator units. Computers & Chemical Engineering 34, 592 – 597. URL: `http://www.sciencedirect.com/science/article/pii/S009813541000030X`, doi:`https://doi.org/10.1016/j.compchemeng.2010.01.017`.

Anton, M., 2013. Egg yolk: structures, functionalities and processes. Journal of the Science of Food and Agriculture 93, 2871–2880. URL: https://onlinelibrary.wiley.com/doi/abs/10.1002/jsfa.6247, doi:10.1002/jsfa.6247, arXiv:https://onlinelibrary.wiley.com/doi/pdf/10.1002/jsfa.6247.

Barnes, H.A., 1994. Rheology of emulsions - a review. Colloids and Surfaces A: Physicochemical and Engineering Aspects 91, 89 – 95. URL: http://www.sciencedirect.com/science/article/pii/092777579302719U, doi:https://doi.org/10.1016/0927-7757(93)02719-U.

Bentley, B.J., Leal, L.G., 1986. An experimental investigation of drop deformation and breakup in steady, two-dimensional linear flows. Journal of Fluid Mechanics 167, 241–283. doi:10.1017/S0022112086002811.

Bird, R.B., Stewart, W.E., Lightfoot, E.N., 1960. Transport Phenomena. John Wiley and Sons, Inc., New York.

Boccardo, G., Marchisio, D.L., Sethi, R., 2014. Microscale simulation of particle deposition in porous media. Journal of Colloid and Interface Science 417, 227–237. URL: https://www.scopus.com/inward/record.uri?eid=2-s2.0-84890195092&doi=10.1016%2fj.jcis.2013.11.007&partnerID=40&md5=03bbbe3c6b053866c5e16eadacc5addf. cited By 34.

Boccardo, G., Sethi, R., Marchisio, D.L., 2019. Fine and ultrafine particle deposition in packed-bed catalytic reactors. Chemical Engineering Science 198, 290–304.

Buffo, A., De Bona, J., Vanni, M., Marchisio, D.L., 2016a. Simplified volume-averaged models for liquid–liquid dispersions: Correct derivation and comparison with other approaches. Chemical Engineering Science 153, 382–393. URL: https://www.scopus.com/inward/record.uri?eid=2-s2.0-84980383589&doi=10.1016%2fj.ces.2016.07.032&partnerID=40&md5=8aad839e2196433ee64beb32429d50eb, doi:10.1016/j.ces.2016.07.032.

Buffo, A., Marchisio, D.L., Vanni, M., Renze, P., 2013. Simulation of polydisperse multiphase systems using population balances and example application to bubbly flows. Chemical Engineering Research and Design 91, 1859–1875. URL: http://www.sciencedirect.com/science/article/pii/S0263876213002645, doi:https://doi.org/10.1016/j.cherd.2013.06.021.

Buffo, A., Vanni, M., Marchisio, D.L., 2016b. On the implementation of moment transport equations in OpenFOAM: Boundedness and realizability. International Journal of Multiphase Flow 85, 223–235. URL: http://www.sciencedirect.com/science/article/pii/S0301932215300525, doi:https://doi.org/10.1016/j.ijmultiphaseflow.2016.06.017.

Bulgarelli, N.A.V., Biazussi, J.L., Monte Verde, W., Perles, C.E., de Castro, M.S., Bannwart, A.C., 2021. Experimental investigation on the performance of Electrical Submersible Pump (ESP) operating with unstable water/oil emulsions. Journal of Petroleum Science and Engineering 197, 107900. URL: https://www.sciencedirect.com/science/article/pii/S0920410520309566, doi:10.1016/j.petrol.2020.107900.

Chesters, A.K., 1991. The modelling of coalescence processes in fluid-liquid dispersions: a review of current understanding. Chemical Engineering Research and Design 69, 259–270.

Chhabra, R.P., Richardson, J.F., 2008. Chapter 1 - Non-Newtonian Fluid Behaviour, in: Chhabra, R.P., Richardson, J.F. (Eds.), Non-Newtonian Flow and Applied Rheology (Second Edition). Butterworth-Heinemann, Oxford, pp. 1–55. URL: https://www.sciencedirect.com/science/article/pii/B9780750685320000019, doi:10.1016/B978-0-7506-8532-0.00001-9.

De Bona, J., Buffo, A., Vanni, M., Marchisio, D.L., 2016. Limitations of simple mass transfer models in polydisperse liquid-liquid dispersions. Chemical Engineering Journal 296, 112–121. URL: https://www.scopus.com/inward/record.uri?eid=2-s2.0-84962319030&doi=10.1016%2fj.cej.2016.03.070&partnerID=40&md5=d0591a4797c2ce41fea5c1b8ae4933d3, doi:10.1016/j.cej.2016.03.070.

Debruijn, R.A., 1991. Deformation and breakup of drops in simple shear flows. Ph.D. thesis. Technische Univ., Eindhoven (Netherlands).

Dubbelboer, A., 2016. Towards optimization of emulsified consumer products : modeling and optimization of sensory and physicochemical aspects. Ph.D. thesis. Technische Universiteit Eindhoven. Department of Chemical Engineering and Chemistry.

Dubbelboer, A., Janssen, J.J.M., Hoogland, H., Zondervan, E., Meuldijk, J., 2016. Pilot-scale production process for high internal phase emulsions: Experimentation and modeling. Chemical Engineering Science 148, 32–43. URL: http://www.sciencedirect.com/science/article/pii/S0009250916301233, doi:https://doi.org/10.1016/j.ces.2016.03.014.

Ferrari, M., Boccardo, G., Marchisio, D.L., Buffo, A., 2023. Application of dissipative particle dynamics to interfacial systems: Parameterization and scaling. AIP Advances 13. URL: https://doi.org/10.1063/5.0139275, doi:10.1063/5.0139275.

Ferrari, M., Handgraaf, J.W., Boccardo, G., Buffo, A., Vanni, M., Marchisio, D.L., 2022. Molecular modeling of the interface of an egg yolk protein-based emulsion. Physics of Fluids 34. URL: https://doi.org/10.1063/5.0079883, doi:10.1063/5.0079883.

Frungieri, G., Boccardo, G., Buffo, A., Karimi–Varzaneh, H.A., Vanni, M., 2022. CFD-DEM characterization and population balance modelling of a dispersive mixing process. Chemical Engineering Science 260, 117859. URL: https://www.sciencedirect.com/science/article/pii/S0009250922004432, doi:https://doi.org/10.1016/j.ces.2022.117859.

Frungieri, G., Boccardo, G., Buffo, A., Marchisio, D., Karimi-Varzaneh, H.A., Vanni, M., 2020. A CFD-DEM approach to study the breakup of fractal agglomerates in an internal mixer. The Canadian Journal of Chemical Engineering 98, 1880–1892. URL: https://onlinelibrary.wiley.com/doi/abs/10.1002/cjce.23773, doi:https://doi.org/10.1002/cjce.23773, arXiv:https://onlinelibrary.wiley.com/doi/pdf/10.1002/cjce.23773.

Frungieri, G., Briesen, H., 2023. A population balance model for the flow-induced preparation of pickering emulsions. Chemical Engineering Research and Design 189, 694–706. URL: https://www.sciencedirect.com/science/article/pii/S0263876222006700, doi:https://doi.org/10.1016/j.cherd.2022.11.037.

Gao, Z., Li, D., Buffo, A., Podgórska, W., Marchisio, D.L., 2016. Simulation of droplet breakage in turbulent liquid–liquid dispersions with CFD-PBM: Comparison of breakage kernels. Chemical Engineering Science 142, 277 – 288. URL: http://www.sciencedirect.com/science/article/pii/S0009250915007642, doi:https://doi.org/10.1016/j.ces.2015.11.040.

Giordano, R.C., Giordano, R.L.C., Prazeres, D.M.F., Cooney, C.L., 1998. Analysis of a Taylor–Poiseuille vortex flow reactor—I: Flow patterns and mass transfer characteristics. Chemical Engineering Science 53, 3635–3652. URL: http://www.sciencedirect.com/science/article/pii/S0009250998001791, doi:https://doi.org/10.1016/S0009-2509(98)00179-1.

Goodarzi, F., Zendehboudi, S., 2019. A Comprehensive Review on Emulsions and Emulsion Stability in Chemical and Energy Industries. The Canadian Journal of Chemical Engineering 97, 281–309. URL: https://onlinelibrary.wiley.com/doi/abs/10.1002/cjce.23336, doi:10.1002/cjce.23336.

Hansen, N., 2006. The CMA Evolution Strategy: A Comparing Review. Springer Berlin Heidelberg, Berlin, Heidelberg. pp. 75–102.

Icardi, M., Gavi, E., Marchisio, D.L., Olsen, M.G., Fox, R.O., Lakehal, D., 2011. Validation of LES predictions for turbulent flow in a Confined Impinging Jets Reactor. Applied Mathematical Modelling 35, 1591–1602. URL: https://www.scopus.com/inward/record.uri?eid=2-s2.0-78650273079&doi=10.1016%2fj.apm.2010.09.035&partnerID=40&md5=207f33f79bb49994da4027060a2d9bb3. cited By 32.

Jansen, K.M.B., Agterof, W.G.M., Mellema, J., 2001. Droplet breakup in concentrated emulsions. Journal of Rheology 45, 227–236. doi:10.1122/1.1333001.

Janssen, J.J., Hoogland, H., 2014. Modelling strategies for emulsification in industrial practice. The Canadian Journal of Chemical Engineering 92, 198–202. URL: https://onlinelibrary.wiley.com/doi/abs/10.1002/cjce.21942, doi:10.1002/cjce.21942.

Klink, I.M., Phillips, R.J., Dungan, S.R., 2011. Effect of emulsion drop-size distribution upon coalescence in simple shear flow: A population balance study. Journal of Colloid and Interface Science 353, 467 – 475. URL: http://www.sciencedirect.com/science/article/pii/S0021979710011100, doi:https://doi.org/10.1016/j.jcis.2010.09.059.

Laakkonen, M., Alopaeus, V., Aittamaa, J., 2006. Validation of bubble breakage, coalescence and mass transfer models for gas–liquid dispersion in agitated vessel. Chemical Engineering Science 61, 218 – 228. URL: http://www.sciencedirect.com/science/article/pii/S0009250905004550, doi:https://doi.org/10.1016/j.ces.2004.11.066.

Lavino, A.D., Ferrari, M., Barresi, A.A., Marchisio, D., 2021. Effect of different good solvents in flash nano-precipitation via multi-scale population balance modeling-CFD coupling approach. Chemical Engineering Science 245, 116833. URL: https://www.sciencedirect.com/science/article/pii/S0009250921003985, doi:https://doi.org/10.1016/j.ces.2021.116833.

Li, D., Gao, Z., Buffo, A., Podgorska, W., Marchisio, D.L., 2017. Droplet breakage and coalescence in liquid–liquid dispersions: Comparison of different kernels with EQMOM and QMOM. AIChE Journal 63, 2293–2311. URL: https://aiche.onlinelibrary.wiley.com/doi/abs/10.1002/aic.15557, doi:10.1002/aic.15557, arXiv:https://aiche.onlinelibrary.wiley.com/doi/pdf/10.1002/aic.15557.

Li, L., Popa, F., Houchens, B.C., 2015. Mechanistic Prediction of Oil-Water, Two-Phase Flow in Horizontal or Near-Horizontal Pipes for a Wide Range of Oil Viscosities, OnePetro. URL: https://onepetro.org/SPEATCE/proceedings-abstract/15ATCE/1-15ATCE/179824, doi:10.2118/174726-MS.

Li, Q.S., Pu, W., Xu, L.x., 2010. Transition to Taylor vortex flow between rotating conical cylinders. Journal of Hydrodynamics, Ser. B 22, 241–245. URL: http://www.sciencedirect.com/science/article/pii/S1001605809600500, doi:https://doi.org/10.1016/S1001-6058(09)60050-0.

Li, X., Zhang, J.j., Xu, L.x., 2014. A numerical investigation of the flow between rotating conical cylinders of two different configurations. Journal of Hydrodynamics 26, 431–435. URL: https://doi.org/10.1016/S1001-6058(14)60049-4, doi:10.1016/S1001-6058(14)60049-4.

Lince, F., Marchisio, D.L., Barresi, A.A., 2011. A comparative study for nanoparticle production with passive mixers via solvent-displacement: Use of CFD models for optimization and design. Chemical Engineering and Processing: Process Intensification 50, 356–368. URL: https://www.scopus.com/inward/record.uri?eid=2-s2.0-79955107468&doi=10.1016%2fj.cep.2011.02.015&partnerID=40&md5=0b3bdc1a42303dfda1abc952a540f1aa. cited By 36.

Lupieri, G., Bagkeris, I., Janssen, J.J., Kowalski, A.J., 2021. Numerical study of a cone mill for emulsion preparation: Hydrodynamics and population balance modelling. Chemical and Process Engineering 42, 295–320.

Maffettone, P., Minale, M., 1998. Equation of change for ellipsoidal drops in viscous flow. Journal of Non-Newtonian Fluid Mechanics 78, 227–241. URL: https://www.sciencedirect.com/science/article/pii/S0377025798000652, doi:https://doi.org/10.1016/S0377-0257(98)00065-2.

Maindarkar, S., Dubbelboer, A., Meuldijk, J., Hoogland, H., Henson, M., 2014. Prediction of emulsion drop size distributions in colloid mills. Chemical Engineering Science 118, 114–125. URL: http://www.sciencedirect.com/science/article/pii/S0009250914003777, doi:https://doi.org/10.1016/j.ces.2014.07.032.

Maindarkar, S.N., Raikar, N.B., Bongers, P., Henson, M.A., 2012. Incorporating emulsion drop coalescence into population balance equation models of high pressure homogenization. Colloids and Surfaces A: Physicochemical and Engineering Aspects 396, 63 – 73. URL: http://www.sciencedirect.com/science/article/pii/S0927775711007874, doi:https://doi.org/10.1016/j.colsurfa.2011.12.041.

Marchisio, D.L., Fox, R.O., 2013. Computational Models for Polydisperse Particulate and Multiphase Systems. Cambridge University Press, Cambridge. URL: https://books.google.it/books?id=SyEAy7zx6zIC.

554 Marchisio, D.L., Omegna, F., Barresi, A.A., Bowen, P., 2008. Effect of mixing and other operating parameters in sol-gel processes. Industrial and
555 Engineering Chemistry Research 47, 7202–7210. URL: https://www.scopus.com/inward/record.uri?eid=2-s2.0-54249129441&
556 doi=10.1021%2fie800217b&partnerID=40&md5=8acd653ef62d97d4bde71a3d47d2f8f2. cited By 39.

557 Marchisio, D.L., Pikturna, J.T., Fox, R.O., Vigil, R.D., Barresi, A.A., 2003a. Quadrature method of moments for population-balance equations.
558 AIChE Journal 49, 1266–1276. URL: https://aiche.onlinelibrary.wiley.com/doi/abs/10.1002/aic.690490517, doi:10.1002/
559 aic.690490517, arXiv:https://aiche.onlinelibrary.wiley.com/doi/pdf/10.1002/aic.690490517.

560 Marchisio, D.L., Vigil, R.D., Fox, R.O., 2003b. Quadrature method of moments for aggregation–breakage processes. Journal of Colloid and
561 Interface Science 258, 322 – 334. URL: http://www.sciencedirect.com/science/article/pii/S0021979702000541, doi:https:
562 //doi.org/10.1016/S0021-9797(02)00054-1.

563 Mazzei, L., Marchisio, D.L., Lettieri, P., 2012. New quadrature-based moment method for the mixing of inert polydisperse fluidized powders in com-
564 mercial CFD codes. AIChE Journal 58, 3054–3069. URL: https://www.scopus.com/inward/record.uri?eid=2-s2.0-84866047786&
565 doi=10.1002%2faic.13714&partnerID=40&md5=349b0e4b8d5c838d05e7023773d1de5a. cited By 34.

566 McClements, D.J., 2005. Food Emulsions: Principles, Practice, and Techniques. CRC Press, Boca Raton, FL.

567 McGraw, R., 1997. Description of Aerosol Dynamics by the Quadrature Method of Moments. Aerosol Science and
568 Technology 27, 255–265. URL: https://doi.org/10.1080/02786829708965471, doi:10.1080/02786829708965471,
569 arXiv:https://doi.org/10.1080/02786829708965471.

570 Noui-Mehidi, M.N., Ohmura, N., Kataoka, K., 2005. Dynamics of the helical flow between rotating conical cylinders. Journal of Fluids and
571 Structures 20, 331–344. URL: http://www.sciencedirect.com/science/article/pii/S0889974605000149, doi:https://doi.
572 org/10.1016/j.jfluidstructs.2004.12.001.

573 Pal, R., 1993. Flow of oil-in-water emulsions through orifice and venturi meters. Industrial & Engineering Chemistry Research 32, 1212–1217.
574 URL: https://doi.org/10.1021/ie00018a029, doi:10.1021/ie00018a029.

575 Pal, R., Hwang, C.Y., 1999. Loss Coefficients for Flow of Surfactant-Stabilized Emulsions Through Pipe Components. Chemical Engineering
576 Research and Design 77, 685–691. URL: https://linkinghub.elsevier.com/retrieve/pii/S0263876299718411, doi:10.1205/
577 026387699526818.

578 Passalacqua, A., Laurent, F., Madadi-Kandjani, E., Heylmun, J.C., Fox, R.O., 2018. An open-source quadrature-based population balance
579 solver for OpenFOAM. Chemical Engineering Science 176, 306–318. URL: http://www.sciencedirect.com/science/article/pii/
580 S0009250917306590, doi:https://doi.org/10.1016/j.ces.2017.10.043.

581 Ramkrishna, D., 2000. Population Balances: Theory and Applications to Particulate Systems in Engineering. Academic Press, London. URL:
582 https://books.google.it/books?id=Ep0N3osDPY4C.

583 Sierra-Pallares, J., Marchisio, D.L., Parra-Santos, M.T., García-Serna, J., Castro, F., Cocero, M.J., 2012. A computational fluid dynamics study of
584 supercritical antisolvent precipitation: Mixing effects on particle size. AIChE Journal 58, 385–398. URL: https://www.scopus.com/inward/
585 record.uri?eid=2-s2.0-80051473422&doi=10.1002%2faic.12594&partnerID=40&md5=4a7a50d5ed1ed62527f2a0404ff458e8.
586 cited By 39.

587 Tosco, T., Marchisio, D.L., Lince, F., Sethi, R., 2013. Extension of the Darcy-Forchheimer Law for Shear-Thinning Fluids and Validation
588 via Pore-Scale Flow Simulations. Transport in Porous Media 96, 1–20. URL: https://www.scopus.com/inward/record.uri?eid=
589 2-s2.0-84870562743&doi=10.1007%2fs11242-012-0070-5&partnerID=40&md5=0c927007bf22f9e2299c10fc2ddb6f80, doi:10.
590 1007/s11242-012-0070-5.

591 Vashisth, V., Nigam, K.D.P., Kumar, V., 2021. Design and development of high shear mixers: Fundamentals, applications and recent progress.
592 Chemical Engineering Science 232, 116296. URL: https://www.sciencedirect.com/science/article/pii/S0009250920308289,
593 doi:10.1016/j.ces.2020.116296.

594 Walstra, P., 1993. Principles of emulsion formation. Chemical Engineering Science 48, 333 – 349. URL: http://www.sciencedirect.com/
595 science/article/pii/000925099380021H, doi:https://doi.org/10.1016/0009-2509(93)80021-H.

596 Wieringa, J.A., Vandieren, F., Janssen, J.J., Agterof, W.G., 1996. Droplet breakup mechanisms during emulsification in colloid mills at high dispersed
597 phase volume fraction. Chemical Engineering Research and Design 74, 554–562. URL: https://www.scopus.com/inward/record.uri?
598 eid=2-s2.0-3042948605&partnerID=40&md5=98df383788284438d110eee7171c1f96.

599 Wimmer, M., 2000. Taylor vortices at different geometries, in: Egbers, C., Pfister, G. (Eds.), Physics of Rotating Fluids, Springer Berlin Heidelberg,
600 Berlin, Heidelberg. pp. 194–212.

601 Wimmer, M., Zierep, J., 2000. Transition from Taylor vortices to cross-flow instabilities. Acta Mechanica 140, 17–30. URL: https:
602 //doi.org/10.1007/BF01175977, doi:10.1007/BF01175977.

603 Zinchenko, A.Z., Davis, R.H., 2015. Extensional and shear flows, and general rheology of concentrated emulsions of deformable drops. Journal of
604 Fluid Mechanics 779, 197–244. doi:10.1017/jfm.2015.411.
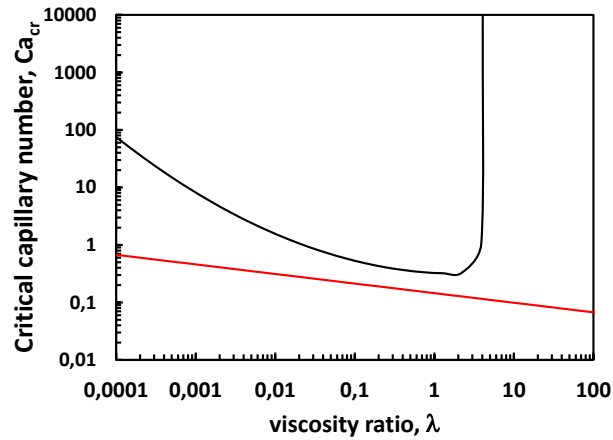
**Figure 1:** Dependency of the critical Capillary number versus the viscosity ratio for pure shear flow (black line $\alpha = 0.5$) and pure elongational flow (red line $\alpha = 1.0$).

**Table 1**

Design of experimental test cases from the work of Dubbelboer (2016); Dubbelboer et al. (2016) and corresponding Reynolds numbers computed in pre-chamber, gap, and post-chambers of the cone mill at oil concentration equal to 0.70 kg/kg (70 wt%).

| Experiment no. | Rotor speed (rpm) | Gap (mm) | Inlet mass flow rate (kg/h) | $Re_{pre}$ | $Re_{gap}$ | | $Re_{post}$ |
|---|---|---|---|---|---|---|---|
| 1 | 6039 | 0.624 | 31 | 12.9 | 140.0 | $> Re_c$ | 212.5 |
| 2 | 6784 | 0.208 | 15 | 12.3 | 61.2 | | 393.4 |
| 3 | 3170 | 0.624 | 64 | 3.7 | 64.6 | | 50.1 |

**Table 2**

Grid independence study on a 2D geometry without pre- and post-mixing chambers for Experiment n. 1 and for a dispersed phase concentration of 0.65 kg/kg.

| | Grid 1 | Grid 2 | Grid 3 | Grid 4 | Grid 5 | Grid 6 |
|---|---|---|---|---|---|---|
| Number of cells along the radial direction | 10 | 15 | 20 | 25 | 30 | 35 |
| Number of cells along the axial direction | 150 | 220 | 285 | 360 | 430 | 500 |
| Total number of cells | 1500 | 3300 | 5700 | 9000 | 12900 | 17500 |
| Number of Taylor vortices | 3 | 16 | 19 | 21 | 21 | 21 |
| Volume-averaged shear rate (1/s) | 28991 | 29733 | 30339 | 30540 | 30605 | 30758 |
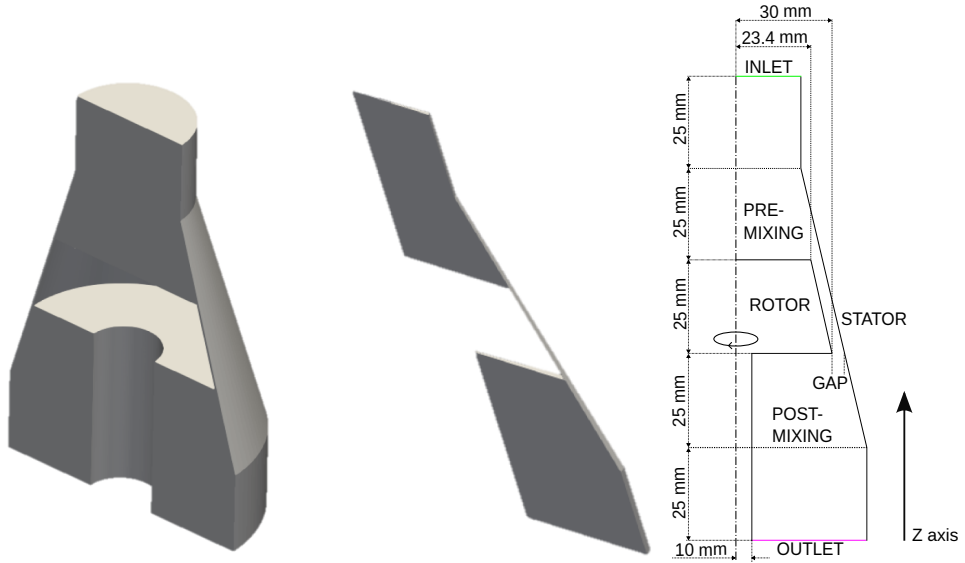
**Figure 2:** Sketch of the cone mill mixer (right) and corresponding 3D (left) and 2D (center) representations.
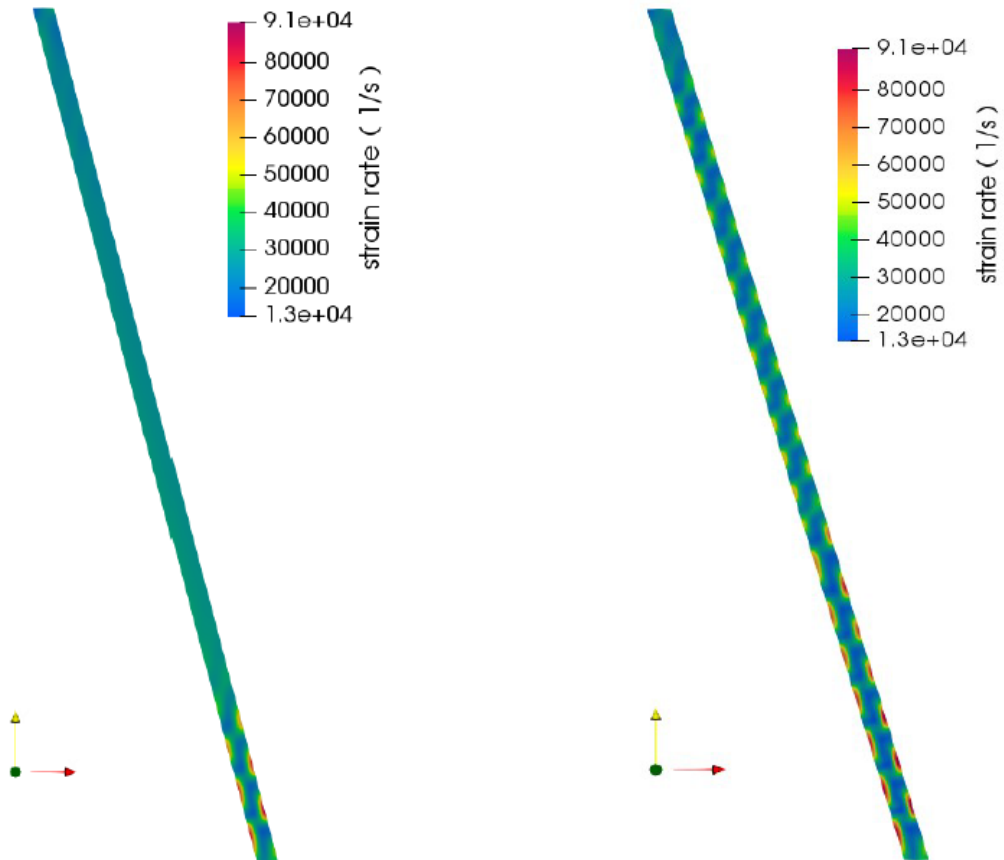


**Figure 3:** Contour plots of the shear rate reported for Experiment 1 and an oil concentration of 0.65 kg/kg for Grid 1 (left) and Grid 4 (right).
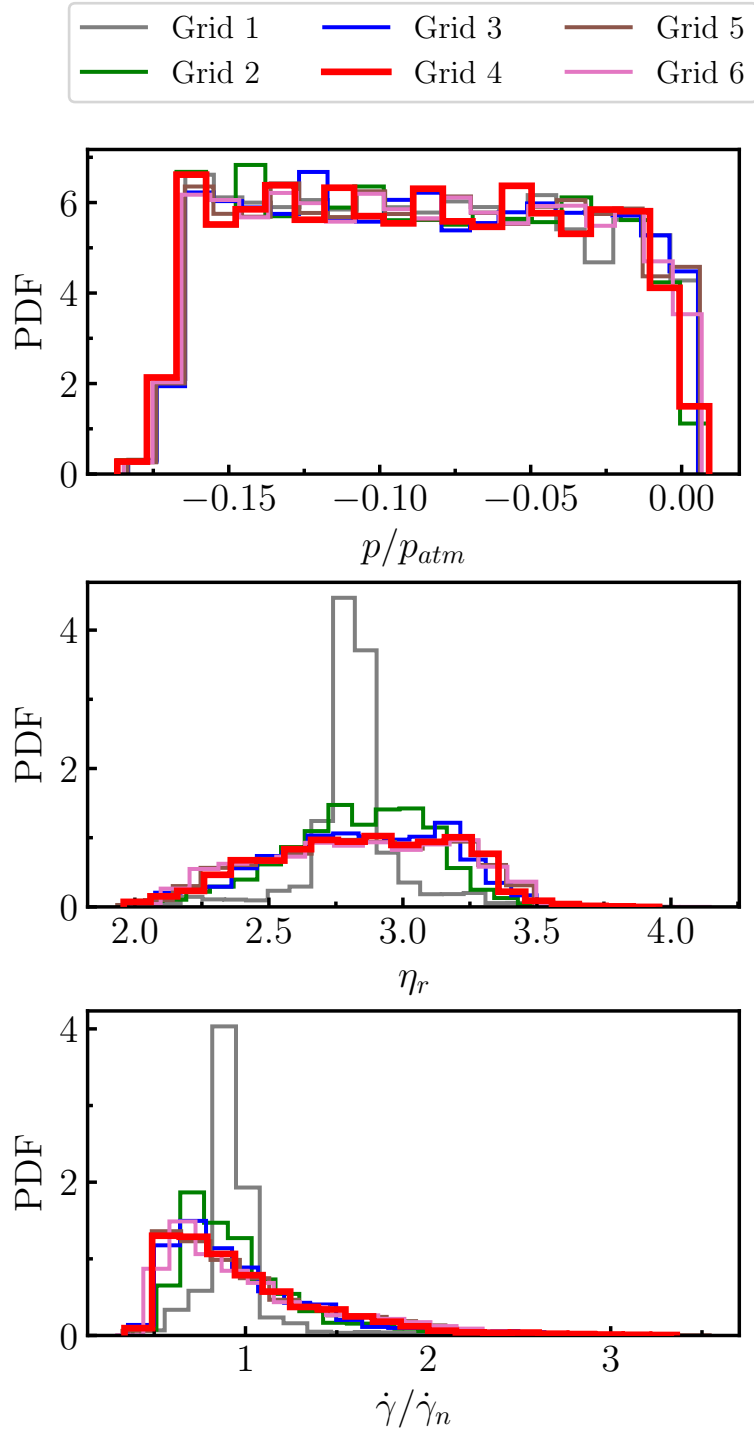
**Figure 4:** Volume probability density distributions (PDF) of the values of normalized pressure $p$, relative viscosity $\eta_r$, and normalized shear rate $\dot{\gamma}$ for different grid resolutions of the gap section for Experiment 1 and for a dispersed phase concentration of 0.65 kg/kg.

**Table 3**

Numerical schemes and boundary conditions used in the simulations.

| Variable | Scheme | Boundary condition | | | |
|---|---|---|---|---|---|
| | | Rotor wall | Stator wall | Inlet | Outlet |
| Pressure | Second-order central scheme | Zero gradient | Zero gradient | Zero gradient | Fixed value |
| Fluid velocity | Bounded second-order upwind | Rotor speed | No-slip | Constant profile | Zero gradient |
| Moments | Bounded first-order upwind | Zero gradient | Zero gradient | Fixed value | Zero gradient |
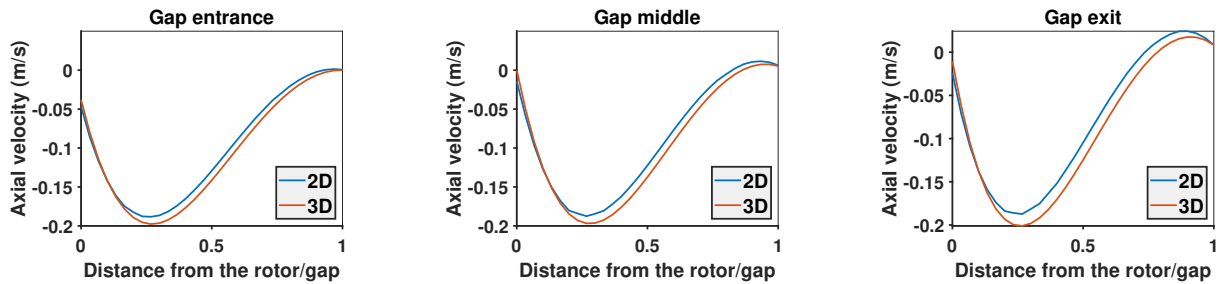


**Figure 5:** Axial velocity across the gap (normalized distance from the rotating wall) at the gap inlet, center, and outlet, as predicted by 2D and 3D simulations for experiment no. 1 and for a dispersed phase concentration of 0.70 kg/kg.
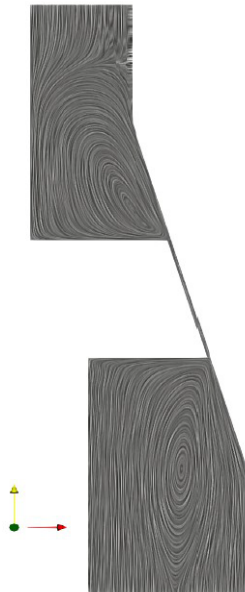


**Figure 6:** Streaklines for experiment no. 1 and for a dispersed phase concentration of 0.65 kg/kg
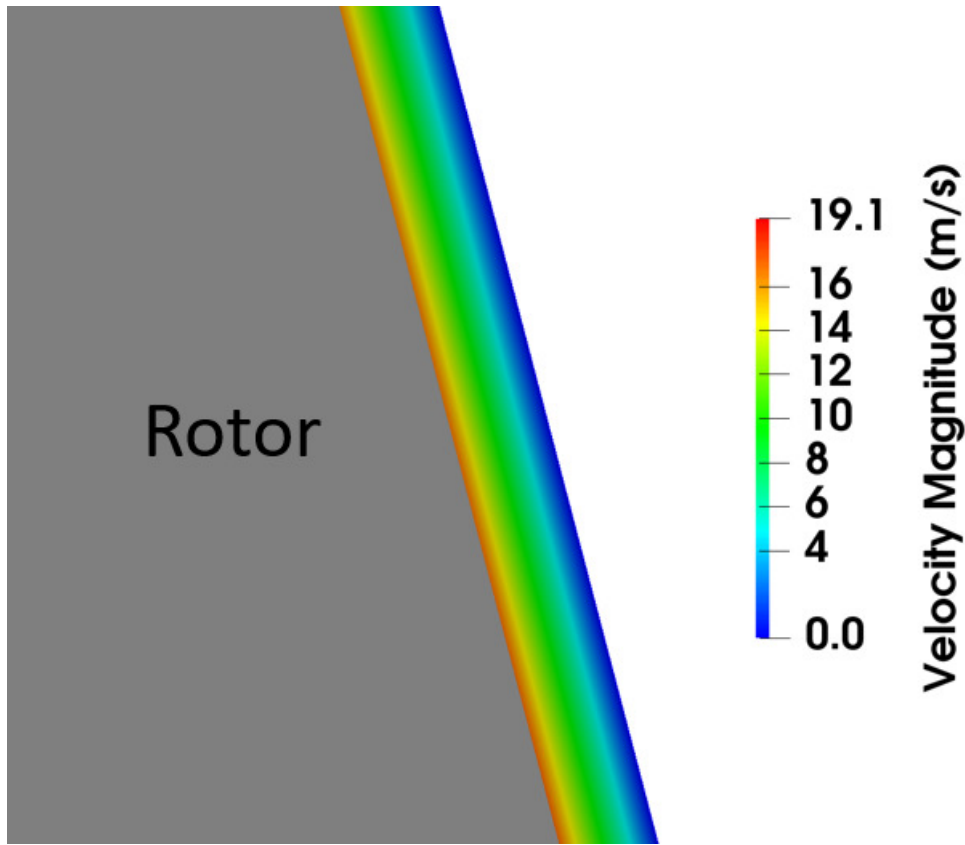
**Figure 7:** Contour plot of the velocity magnitude in a magnified longitudinal section of the cone mill with oil concentration equal to 0.70 kg/kg (70 wt%) and at operating conditions corresponding to experiment no. 1 (see Table 1).

**Table 4**

Comparison between PBM predictions and experimental measurements for the mean Sauter diameter for experiments no. 1 and 3 for different values of the coalescence kernel constants, $K_1$ and $K_2$, and the breakage kernel constants, $K_3$ and $K_4$.

| Experiment | $K_1$ | $K_2$ | $K_3$ | $K_4$ | $d_{32}^{Model}(\mu m)$ | $d_{32}^{Exp}(\mu m)$ |
|---|---|---|---|---|---|---|
| | $1 \times 10^{-6}$ | $1.077 \times 10^2$ | $2.154 \times 10^{-4}$ | $1.744 \times 10^{-3}$ | 6.9 | |
| no. 1 | $2.154 \times 10^{-4}$ | $1.498 \times 10^{-6}$ | $4.642 \times 10^{-2}$ | 2.684 | 3.6 | 6.6 |
| | $1 \times 10^1$ | $1.077 \times 10^2$ | $2.154 \times 10^{-4}$ | 2.684 | 23.7 | |
| | $1 \times 10^{-6}$ | $1.077 \times 10^2$ | $2.154 \times 10^{-4}$ | $1.744 \times 10^{-3}$ | 29.1 | |
| no. 3 | $2.154 \times 10^{-4}$ | $1.498 \times 10^{-6}$ | $4.642 \times 10^{-2}$ | 2.684 | 6.7 | 7.7 |
| | $1 \times 10^1$ | $1.077 \times 10^2$ | $2.154 \times 10^{-4}$ | 2.684 | 32.0 | |
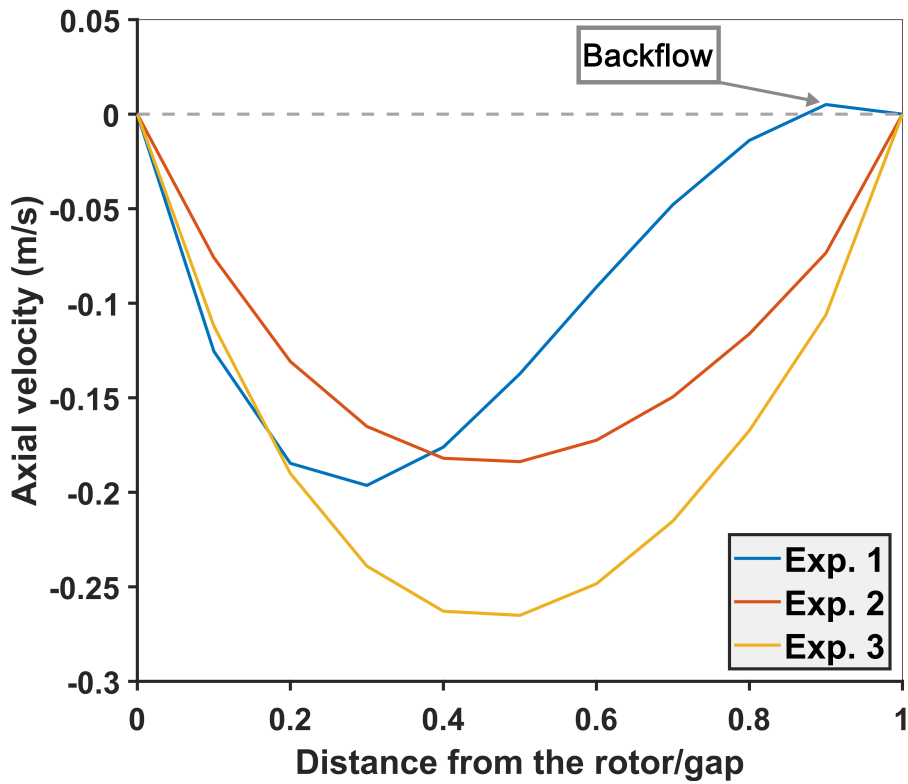
**Figure 8:** Axial velocity profiles versus the normalized distance from the rotor wall at half height of the cone mill with oil concentration equal to 0.70 kg/kg (70 wt%) and for different operating conditions (see Table 1).

**Table 5**

The final comparison between the mean Sauter diameter predicted by the PBM and measured experimentally for experiments no. 1, 2, and 3 and for the three dispersed phase concentrations investigated in this work.

| Exp. | Mayonnaise 1 (0.65 kg/kg) | | Mayonnaise 2 (0.70 kg/kg) | | Mayonnaise 3 (0.75 kg/kg) | |
|---|---|---|---|---|---|---|
| | exp. data [$\mu$m] | model pred. [$\mu$m] | exp. data [$\mu$m] | model pred. [$\mu$m] | exp. data [$\mu$m] | model pred. [$\mu$m] |
| 1 | 7.206 | 9.530 | 6.587 | 5.180 | 4.647 | 3.180 |
| 2 | 8.787 | 9.250 | 5.844 | 4.780 | 4.815 | 2.950 |
| 3 | 12.364 | 11.99 | 7.713 | 6.130 | 6.063 | 3.830 |
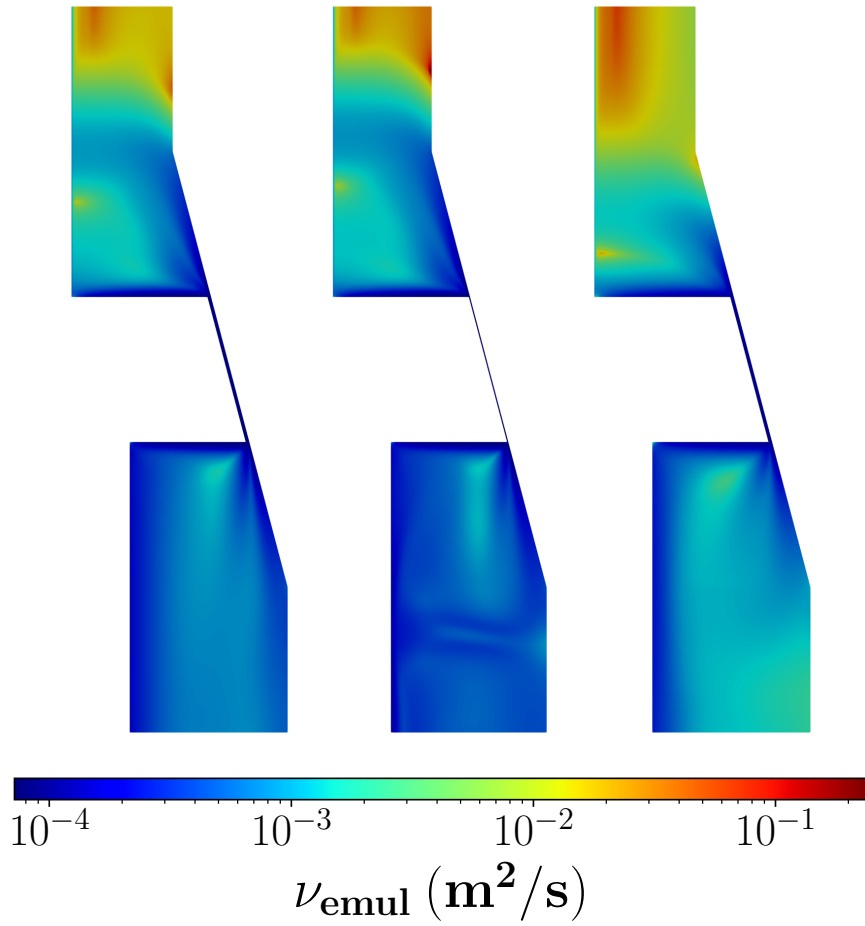
**Figure 9:** Contour plots of the emulsion apparent kinematic viscosity $\nu_{emul}$ corresponding to experiment no. 1 (left), 2 (center), and 3 (right) of Table 1 at an oil concentration equal to 0.70 kg/kg.
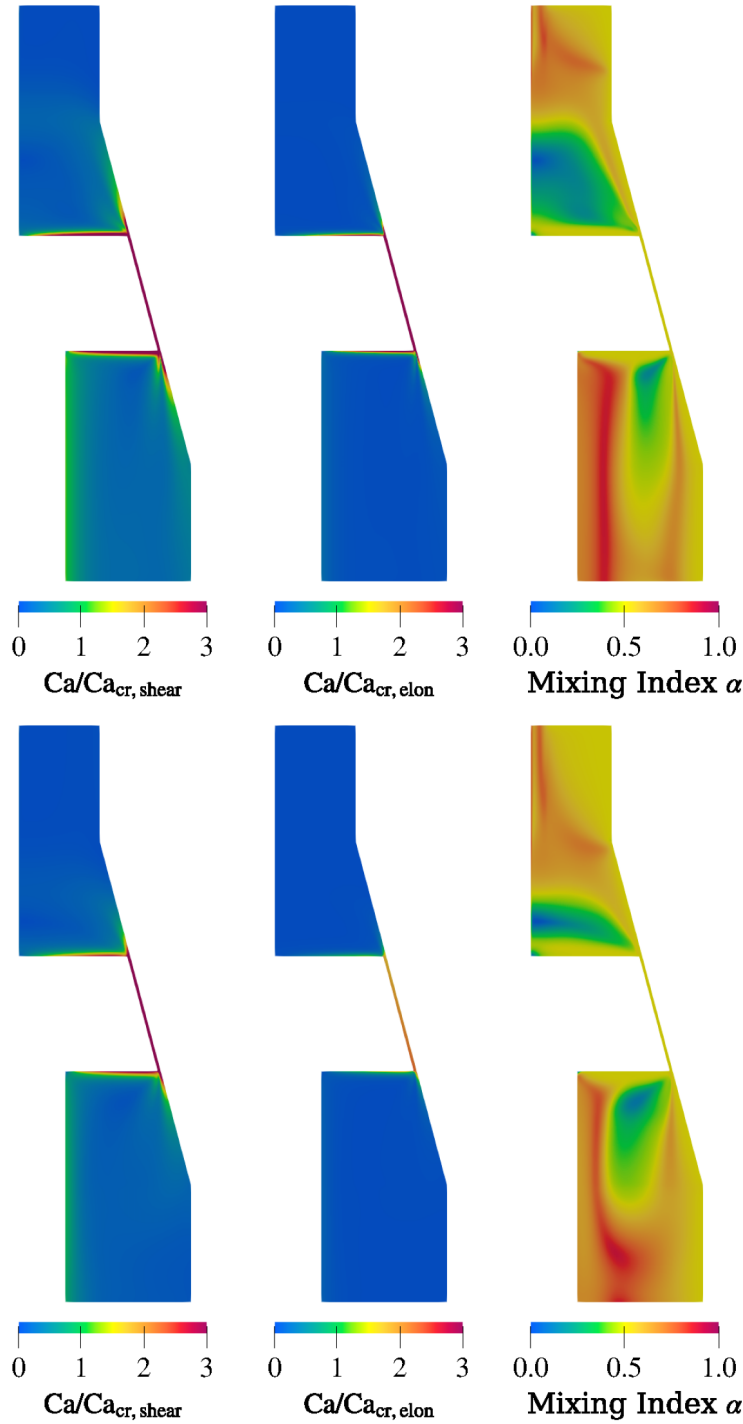
**Figure 10:** Contour plots for the ratio between the Capillary number and the critical Capillary number calculated by using the emulsion viscosity and Eq. (11) (left) and the continuous phase viscosity and Eq. (12) (center), and the mixing index $\alpha$ (right) for Experiment no. 1 (top) and no. 3 (bottom) and an oil concentration of 0.70 kg/kg.
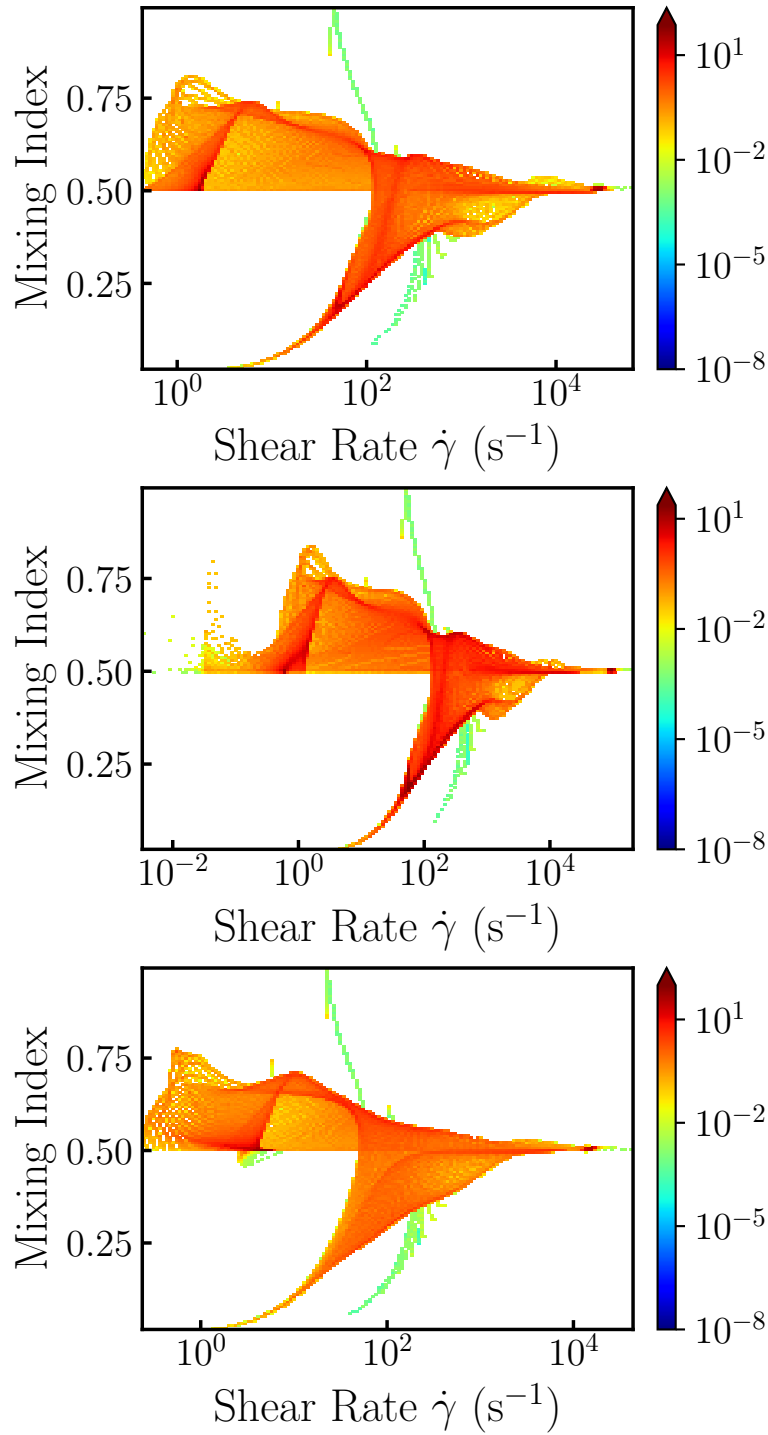
**Figure 11:** Volume distribution of mixing index (-) and shear rate (1/s) for operating conditions corresponding to experiment no. 1 (top), no. 2 (middle), and no. 3 (bottom) and an oil concentration of 0.70 kg/kg.
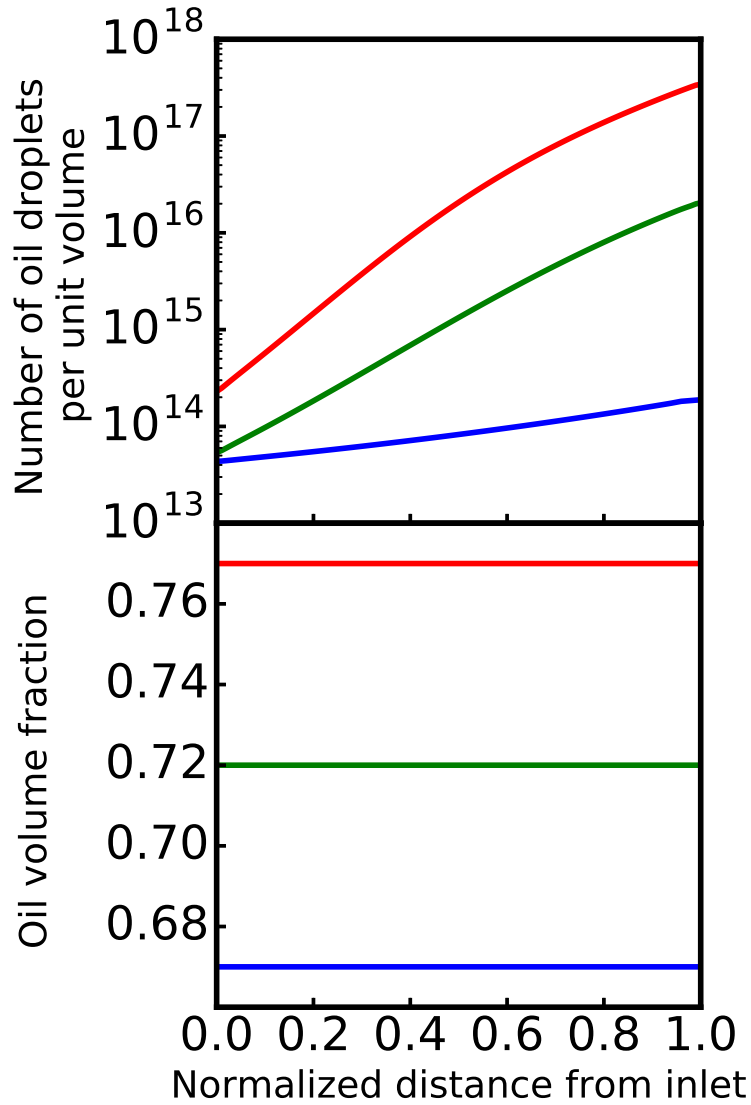
**Figure 12:** The trend of the number of oil droplets per unit volume ($M_0$, top) and oil volume fraction ($\pi/6M_3$, bottom) along the normalized distance from the middle point of the inlet to the middle point of the outlet of the cone mill mixer, for oil concentrations equal to 0.65 kg/kg (blue line), 0.70 kg/kg (green line), and 0.75 kg/kg (red line) in the experiment n.3 (see Table 1).
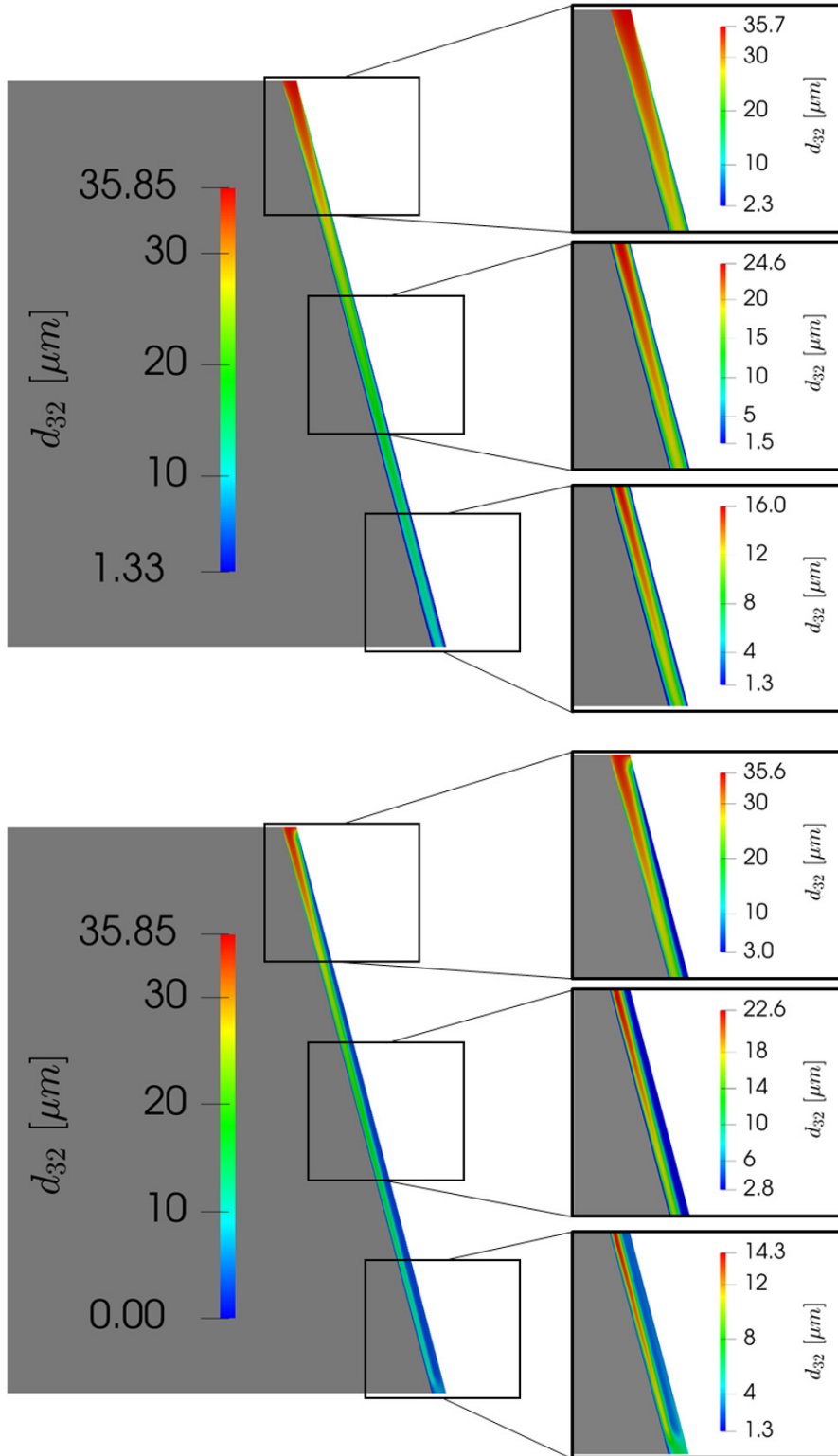
**Figure 13:** Contour plots of the mean Sauter diameter $d_{32}$ of oil droplets along a longitudinal section of the cone mill with oil concentration equal to 0.70 kg/kg (70 wt%) for the experiments n. 3 (top) and n. 1 (bottom) (see Table 1). Insets are magnified gap sections.
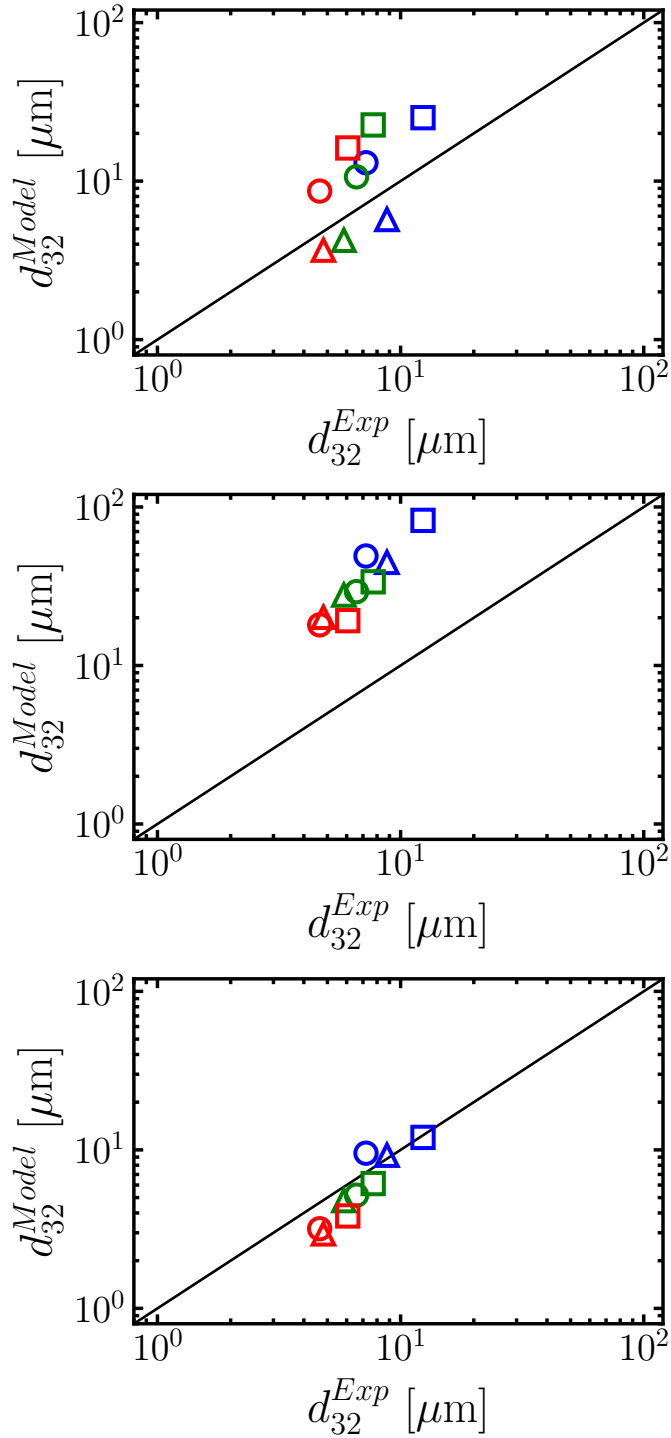
**Figure 14:** Comparison between the outlet experimental Sauter mean diameter values and the predicted ones for Experiments no. 1, 2, and 3 (circle, triangle, and square symbols, respectively) and oil content of 0.65 kg/kg, 0.70 kg/kg, and 0.75 kg/kg (blue, green, and red symbols, respectively) when droplet breakage occurs due to the simple shear (top), elongational flow (middle), and the combination of both of them (bottom).